Extreme Southwest U.S. and Northern Mexico Vapor Pressure Deficit Events in CMIP6 Climate Model Projections

David Gregory Lopez

A thesis

submitted in partial fulfillment of the

requirements for the degree of

Master of Science

University of Washington

2025

Committee:

Dargan Frierson

Becky Alexander

Dennis Hartmann

Program Authorized to Offer Degree:

Atmospheric and Climate Science

University of Washington

Abstract

Extreme Southwest U.S. and Northern Mexico Vapor Pressure Deficit Events in CMIP6 Climate Model Projections

David Gregory Lopez

Chair of the Supervisory Committee:

Dargan Frierson

Department of Atmospheric and Climate Science

This study characterizes the most extreme events of vapor pressure deficit (VPD) in CMIP6 SSP5-8.5 projections for nine different climate models in the greater Southwest U.S. and Northern Mexico region. VPD is a strong predictor of wildfire area burned in Southwestern North America. Model base states are in spatial agreement for temperature and moisture to observational studies. Two areas of VPD are present with differing dominant terms in VPD formulation. Individual event extremities also have differing dominant terms. Precipitation hinders the evolution and magnitude of VPD extremities. Maximum yearly VPD takes place prior to maximum yearly solar insolation in all models, just prior to precipitation of the expected North American Monsoon. Among all extreme events, a minimal precipitation signal is present in the period prior.

Table of Contents

1. Introduction

Despite a fairly constant number of wildfires in the U.S., the area of land burned by wildfires has increased steadily since 1983 (1983, when federal wildland fire agencies adopted current wildfire reporting processes), and increased by nearly a factor of 4 to near present time (Nasa, Accessed 03/13/2025). This is contrary to the global trend of decreasing area burned, and in further disparity, U.S. federal costs of wildfire suppression have risen substantially (Jaffe et al., 2020).

The Canadian Fire Weather Index (FWI) represents potential fire danger (Van Wagner, 1987) and has been widely used for the U.S. and Canada (e.g., Liu et al, 2024). FWI is based on a complex set of nonlinear equations involving meteorological fields and the moisture content of different types of fuel. The empirical tuning, nonlinearity, and complexity of the FWI expression make it difficult to interpret within a climate model, especially under large climate changes. Instead, vapor pressure deficit (VPD) can easily be calculated within climate models, and has been shown to be a strong proxy for wildfire area burned. This includes the Southwest U.S., with some careful considerations, where VPD has increased in the Southwest U.S. since 1961 (Seager et al. 2015). VPD also has the advantage in measuring the effects of atmospheric moisture on conditions upon living organisms (Anderson, 1936). VPD has a strong temperature dependence, so is expected to increase with global warming. Changes of VPD have been attributed to changing temperature, dynamical changes (with temperature and humidity contributions), and humidity changes (Hermann et al., 2024).

1.1. Research Purpose

The goal of this study is to broadly understand events of extreme VPD in the arid Southwest U.S. and Northern Mexico. Specifically, I utilize the CMIP6 SSP5-8.5 projections, where the highest level of greenhouse gas forcing is present (Meinshausen et al., 2020), to analyze the highest projected events of VPD in this region. In this region, VPD is already the most extreme in the US, is projected to increase the most, and has the greatest anomalies (Seager et al., 2015).

Questions posed in this study include: Is there a build-up of high VPD leading into an event of highest VPD?; Does a continual drying of soil lead to high VPD events (the actual vapor pressure dominating high VPD), or does an anomalously high temperature imposed by a rather sudden meteorological event allow for high VPD events (the saturated vapor pressure dominating high VPD)?

1.2. Structure of the Masters Thesis

This Masters Thesis begins with a literature review in Section 2, on five key aspects important to understanding the projections of extreme vapor pressure deficit events in the Southwest U.S. and Northern Mexican region. I start in Section 2.1 by introducing the nine CMIP6 climate models used in this study under ScenarioMIP SSP5-8.5. I then define the Southwest U.S. and Northern Mexico region by its geography and climatology in Sections 2.2 and 2.3. Section 2.4 gives special interest to the North American Monsoon which is present in this region during which the temperatures in this region are the most extreme (positive; leading to exponentially higher saturation vapor pressures). As I am studying VPD, Section 2.5 discusses literature relevant to VPD in Southwestern North America.

Following the literature review, Section 3 presents the data and methods used in this study. This includes, in Section 3.2, a qualitative definition of VPD, discussion of different formulations of vapor pressure and methods of averaging to approximate VPD, and the formulation for VPD used in this study. Section 3.3 presents the CMIP6 meteorological variables used in this study, followed by Section 3.4 with a description of isoplething methods utilized for plotting.

In section 4 I present an analysis and discussion of my results. Section 4.2 defines extreme VPD events, introducing the three most extreme cases of VPD within each model. Section 4.3 includes a spatial description of select meteorological variables in regards to their climatological change within each model. Section 4.4 then analyzes the extreme VPD cases temporally, with a description of VPD and related meteorological variable climatology within each model, followed by a thorough description of the evolution for the three most extreme cases of VPD within each model.

Ultimately this research allows me to qualitatively describe the meteorological conditions present in CMIP6 SSP5-8.5 experiments that lead to the most extreme cases of vapor pressure deficit in this region, and North America.

2. Literature Review

2.1. CMIP6 and ScenarioMIP SSP5-8.5

In this study, I use nine CMIP6 models based upon data availability for the research scope of this study. An in-depth discussion of the data used from CMIP6 is discussed in subsequent sections. CMIP6 is the sixth phase of the Coupled Model Intercomparison Project, designed in expectation of supporting the Intergovernmental Program on Climate Change's (IPCC) Sixth Assessment Report (Eyring et al., 2016). Broad questions intended for CMIP6 to address include:

- "How does the Earth system respond to forcing?
- What are the origins and consequences of systematic model biases?
- How can we assess future climate changes given internal climate variability, predictability, and uncertainties in scenarios?"

CMIP6 has 21 endorsed MIPs (Model Intercomparison Projects). In this study I investigate the SSP5-8.5 scenario from the "ScenarioMIP" (O'Neill et al., 2016). ScenarioMIP is the primary activity within CMIP6, providing "multi-model climate projections based on alternative scenarios that are directly relevant to societal concerns regarding climate change mitigation, adaptation, or impacts." "SSP5" represents pathways with fossil-fueled development, and "8.5" represents pathways with a 2100 forcing level of 8.5 W/m2. SSP5-8.5 is a fossil-fueled scenario with the greatest level of projected forcing within ScenarioMIP.

Climate models have different methods of modelling the physics of the Earth system. This is what leads to variance among models. In consequence, the base state of each model must vary, in that the base state (initial conditions) of each model is physically representative of the dynamics defining each model. To accomplish this, CMIP6 ScenarioMIP model runs use CMIP6 "historical" outputs as their initial, base state. CMIP6 historical simulations (Eyring et al., 2016) are run from the year 1850 through 2014, have the same physics embedded as ScenarioMIP, and are given boundary forcing conditions.

2.2. Geographical Considerations

To properly understand the meteorological influence on VPD in this region, considerations of the natural physical geography must be taken. Figure 2.2.1 displays the boxed area of interest for this study (further defined by model in Section 3.2.1), where the color scheme represents topography in kilometers (km). A common misconception with this region is the assumption of a lack of vegetation (wildfire fuel). Despite the major deserts in this region, there is no lack of vegetation (Hafner and Riddle, 2011).

Arguably, the most important feature to consider in this study is a location's relation to water sources. Section 2.4 covers the North American Monsoon, a phenomenon that brings much of this region's warm season precipitation. North American Monsoon moisture originates from the Gulf of California at low pressure levels, and from the Gulf of Mexico as a secondary source at high pressure levels (Adams and Comrie, 1997).

Topography plays an important role in a location's climate. Lower-lying places will tend to have warmer surface temperatures, while places at higher elevation tend to have lower surface temperatures. Phoenix, Arizona is located just northeast of the northernmost part of the Gulf of California. San Diego, California is located at the southwest corner of the U.S. along the Pacific coastline. South of San Diego lies the Baja California Peninsula, with Mexican states Baja California and Baja California Sur, extending south-southeast with coastline on the Pacific Ocean and the Gulf of California. The Southern tip of the Peninsula lies the city of La Paz, Baja California Sur. Opposite of La Paz lies the state of Sinaloa with cities Mazatlán and Culiacán, and opposite of the Baja California/Baja California Sur border lies the city of Hermosilla, Sonora. Hermosilla, Mazatlán, and Culiacán all lie along the Gulf of California, and are just west of the Sierra Madre Occidental.

All of the locations mentioned so far are low-lying, and to the west of major mountain ranges and plateaus. Las Vegas, Nevada is also rather low-lying and to the West of the Colorado Plateau. Death Valley, California is in the Mojave Desert, exemplifying the effects of low elevation on extreme temperatures, holding Earth's world record highest temperature at 56.7 °C, (World Meteorological Organization; Accessed 05/28/2025). Less of a focus in this study but still in the region of interest is California's low-lying Central Valley.

The Sierra Madre Occidental is a high elevation and widespread feature extending through central Mexico, decently defining the spread of the Chihuahuan Desert. North of this, in the US, lies the Colorado Plateau, part of the greater Rocky Mountains extending far north through Wyoming, the western part of Montana, and into Canada. Gallup, New Mexico, and the infamous Four Corners lie in this part. Further west lies the Great Basin, east of the Sierra Nevada Mountains (eastern border of California's Central Valley), and also a high elevation area with a wide extent just North of Death Valley and Las Vegas. The border of the Rocky Mountains has the cities of Denver, Colorado and Santa Fe, New Mexico, before elevation begins to slowly decrease into the loosely defined Great Plains region.

The eastern part of this region is loosely defined (for all intents and purposes) as the Great Plains. This is a low lying region, relative to the high elevation mountain ranges to the west. Nevertheless, some mandatory pressure levels (1000 mb, and sometimes 850 mb) are theoretical (levels are produced with assumptions, such as a constant lapse rate) even in this loosely defined Great Plains. Some cities in this region include San Antonio, Texas in central Texas, Amarillo, Texas in the Texas panhandle, and Hays, Kansas.

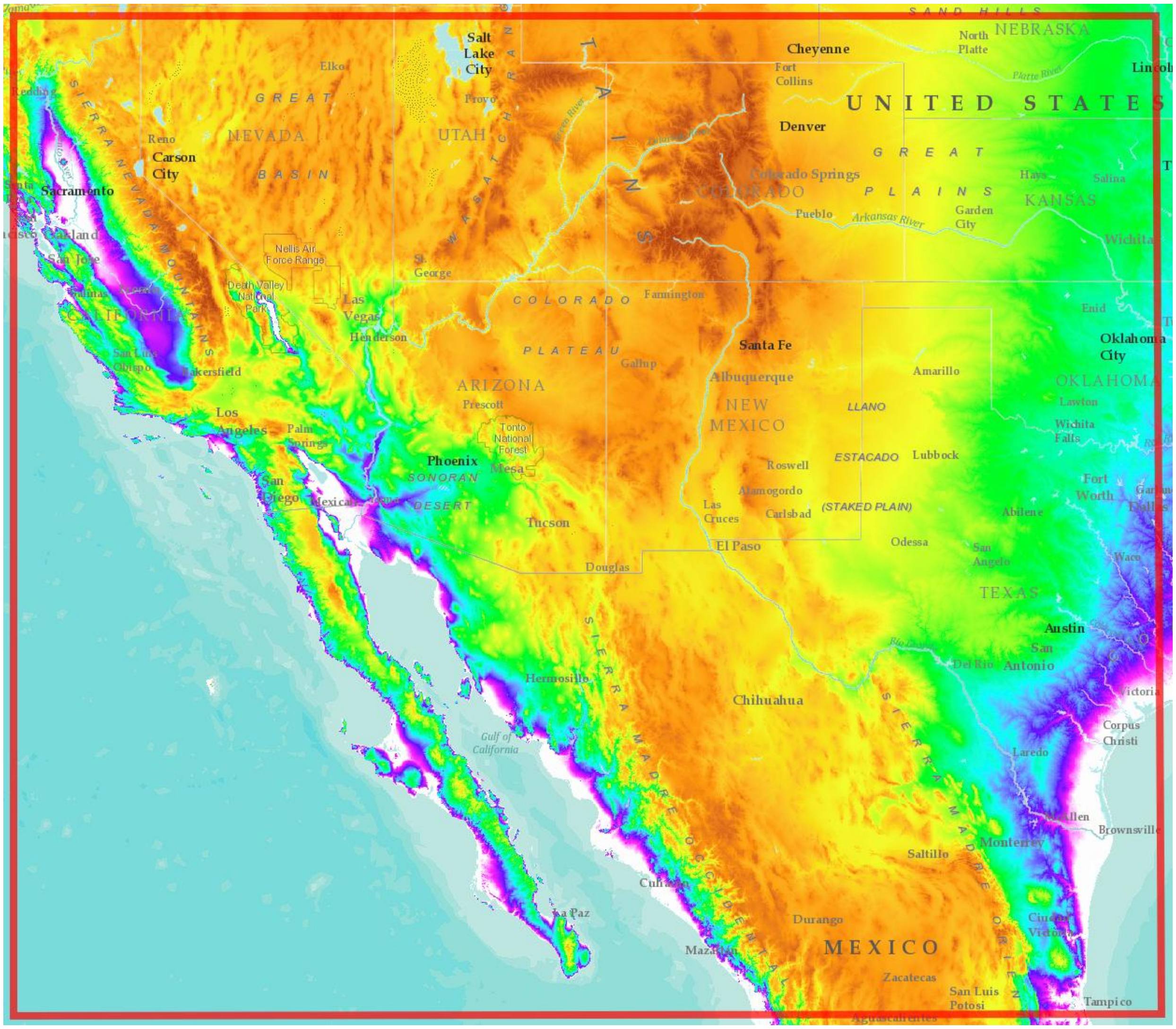

Figure 2.2.1. Topography Map. (Conservation Biology Institute, https://databasin.org/maps/new/#datasets=588bcc4e1f2646e589e0fc9593498e3d, Accessed 06/01/2025). Map contains the region of interest for this study of the Southwest U.S. and Northern Mexico. Displayed in color is topography with data originating from the U.S. Geological Survey. High elevation is in red, and low elevation is in white.

2.3. Climatology

The Southwest U.S. is prone to heat and limited precipitation (Sheppard et al., 2002). Despite the common idea of a region in close proximity to large bodies of water being less susceptible to temperature extremes, the low-lying Sonoran Desert that wraps around the Gulf of

California experiences some of North America's warmest temperatures. Most of the lower elevation zones of the monsoon region (defined in section 2.4), particularly the Sonoran Desert, receive up to 80% or 90% of possible summer insolation, and have surface temperatures often exceeding 40 °C (Adams and Comrie, 1997).

Warm season precipitation and their forcing mechanisms are very different from their cool season counterparts in the Southwest U.S. (Ciancarelli et al., 2013). A monsoonal ridge is present during the warm season. The monsoon in the Southwest is early and wet when the ridge is positioned north/northeast to its climatological position, and late and dry when the ridge is suppressed to the south with a trough over the West (Carleton et al., 1990). Cool season precipitation in the Southwest is principally influenced by large-scale forcing from the combination of the El Nino Southern Oscillation and Pacific Decadal Oscillation (Gutzler et al., 2002). During an El Nino event, cool season processes in the atmosphere tend to lead to more frequent and intense midlatitude cyclones with wetter than average winters (Wallace and Gutzler, 1981; Mo and Paegle, 2000).

At time of publication, Williams et al. (2022) showed Southwestern North America to be in a "megadrought," with the driest 22-year period (2000 through 2021) since at least the year 800. Droughts are monitored in the U.S. using "The Drought Monitor" (Svoboda et al., 2002), where drought levels are categorized by several indicators with corresponding percentiles for chance of occurrence in any given year within a 100-year period. During this event, precipitation was 8.3% below average while temperature was 0.91 °C above average (average: years 1950–1999), and approximately 19% of soil moisture deficit was attributable to anthropogenic climate trends. Their spatial extent of drought was widespread across the western US, with maximum drought present in Arizona through the Four Corners and across the Colorado Plateau. A study by Soulé and Knapp (2024) investigated the evolution of droughts in the Southern California parts of the Sonoran Desert, Mojave Desert, and Great Basin since the beginning of the 20th century. Concurrent with anthropogenic warming trends, Soulé and Knapp found that droughts are stronger, longer, and more frequent in the 21st century.

In the following paragraphs, I evaluate ERA5 Reanalysis data (Hersbach et al., 2023) for important locations mentioned in Section 2.4.1, describing the spatial extent of temperature, precipitation, and winds in my region of interest (Generated using Copernicus Climate Change Service information [2025]). Considering these descriptions is important for understanding the trends present in CMIP6 projections.

On the border of Baja California and Baja California Sur, temperature rises to its yearly maximum in June with an average maximum temperature of 35.1 °C. Precipitation is prevalent from August through March with no less than 6.5 mm/month, while April through July are about 2 mm/month or lower. Starkly in August, precipitation rises from 2.2 to 10 mm with a maximum of 20 mm in September. Many locations in this region show similar temperature and precipitation trends. To name a few: Phoenix's highest average monthly maximum temperature is in July at 41.4 °C with precipitation rising from 2.1 mm to 20 mm in July and 31 mm in August. Hermosillo's highest average monthly maximum temperature is in June at 39.4 °C with precipitation rising from 3.9 mm in June to 43 mm in July and 54 mm in August. Culiacan's highest maximum monthly temperature is in June at 36.3 °C with precipitation, much higher, rising from 28 mm in June to 160 mm in July and 190 in August. Santa Fe's highest maximum monthly temperature is more modest, in July at 28.6 °C, with a more modest increase in precipitation from the June minimum at 17 mm to 37 mm in July and 38 mm in August. Chihuahua City, on the Sierra Madre Occidental, has a highest maximum monthly temperature of 34.8 °C in June with precipitation rising from 22 mm to 70 mm in July and 69 mm in August.

In general, despite the broad extent of the North American deserts in the Southwest U.S. and Northern Mexico and their often distant relation to moisture sources, these regions have monsoon-like precipitation that tends to begin in mid-Summer lasting through early Autumn. Cities that show this behavior also generally have their month of temperature maximum in the month preceding a stark increase in precipitation.

Winds are generally present from the north-northwest, flowing through the Gulf of California. In the mid-year months of June and July, winds switch directions, rotating cyclonically around the Baja California peninsula, through the Gulf of California, ultimately converging with winds from the Gulf of Mexico near the New Mexico-Texas border. In later months, the convergence occurs further to the north.

The Bay Area (San Francisco) and California's Central Valley have predominant wintertime precipitation. Their highest maximum monthly temperatures are 19.8 °C in September and 33.7 °C in July, respectively. San Diego is similar with wintertime precipitation, and has a highest maximum monthly temperature in August at 23.5 °C. In general, coastal California and the parts of California west of the Sierra Nevada Mountains follow the trend of wintertime precipitation with more moderate maximum temperatures relative to the desert cities.

Further North and into the loosely defined Great Plains region, Amarillo shows a broad mid-year precipitation maximum at 63 mm in both May and August, Denver shows a broad late Spring precipitation maximum at 86 mm in May, and Hays shows a broad mid-year maximum precipitation with a maximum of 110 mm in May. All three of these places have very similar highest maximum monthly temperatures, being in July for all three at 33.2 °C, 33.3 °C, and 33.6 °C respectively. San Antonio, closer to the Gulf of Mexico, still shows a late summer increase in precipitation from 53 mm in August to 82mm and 86 mm in September and October respectively, and a highest maximum monthly temperature of 35.3 °C in August. However, San Antonio also has a broad late Spring maximum precipitation of 110 mm in May.

2.4. North American Monsoon

Special focus on the North American Monsoon (NAM) is given in this section, providing a significant moisture source to my region of interest during the warm season (Adams and Comrie, 1997). The NAM is expected to influence the vapor pressure term of VPD during or near the season at which saturated vapor pressure is at its maximum (hottest temperatures climatologically).

By definition, a monsoon literally means “rainy season,” and is characterized by a seasonal reversal in atmospheric low-level circulations associated with precipitation leading to dry winters and rainy summers (American Meteorological Society, Accessed 05/28/2025). As described in Adams and Comrie's (1997) review of NAM literature, the NAM is characterized as a phenomenon centered over Northwestern Mexico (where it has its greatest influence) that extends into most Southwestern U.S. states. Monsoonal moisture and tendency for severe thunderstorms has been shown in some studies to be greatest in New Mexico and Arizona, although a disproportionate number of studies have focussed solely on this region. Historically one of the identifying names used for the NAM was the Arizona monsoon, however the area affected by the NAM is significantly greater than Arizona.

A general consensus amongst past researchers for the cause of the monsoon is a subtropical ridge providing anticyclonic circulation that advects moisture primarily from the Gulf of California, with some upper-level moisture from the Gulf of Mexico (Adams and Comrie, 1997). The Gulf of California is believed to be the primary source of moisture, and the Gulf of Mexico is confirmed to be an upper level influence of moisture due to the high elevation of the Sierra Madre Occidental where pressure levels of about 800/850 mb are sometimes theoretical. With the combination of seasonally warm surface temperatures and nearby maritime sources for atmospheric moisture, this region is conducive to forming monsoonlike systems.

Seasonally, the NAM is characterized as a "pronounced increase in rainfall from an extremely dry June to a rainy July," that typically lasts through mid-September (Adams and Comrie, 1997). The NAM is associated with severe thunderstorms (Maddox et al., 1995), including cloud to ground lightning, and dust storm generation (Brazel and Nickling, 1986). Sea surface temperatures in the Gulf of California and tropical Eastern Pacific are considered hot (> 28 °C) with sea surface temperatures on the opposite side of Mexico also being considered hot (>

26 °C) in the Gulf of Mexico (Adams and Comrie, 1997). A Gulf surge refers to a "burst" of moisture originating from the Gulf of California typically confined below the 700mb pressure level that is driven northward by a thermal low in the hot deserts of Arizona and Southeastern California. Major surges are thought to originate from increased subsidence from a midlatitude trough passing through in the 1 to 3 days prior to an easterly wave (Stensrud et al., 1997).

The effect of climate modes on the NAM's warm season behavior remained elusive for some time (Adams and Comrie, 1997), however a 2011 study by Ciancarelli et al. suggests that La Nina conditions tend to favor more robust monsoons with El Nino conditions favoring less active monsoons.

2.5. Southwestern VPD

Continuing with a description of Southwest North American climatology, VPD is an "accurate metric of the ability of the atmosphere to extract moisture from the land surface" (Seager et al., 2015). Seager et al., have shown the spatial extent of VPD in the U.S. by season for the 1961 to 2012 period. In a region defined similarly to the NAM, and my region, however limited by the Southern U.S. border and ending to the north, just north of the Four Corners, June through August VPD shows a strong correlation to wildfire area burned on a logarithmic scale ($r = 0.80$). VPD is at a minimum during the Winter (Jan. - Mar.) and maximum during the Summer (Jul. - Sept.) with a region of maximum VPD in the Sonoran Desert. The low-lying area East of the Rockies (broadly defined as the Great Plains in this study) shows a broad extent of moderate VPD in relation to the Sonoran Desert. These two regions also have the highest VPD variances. However, the Southwest (including the Sonoran Desert with a broader extent) shows low standard deviation divided by the climatology for VPD, while high for actual vapor pressure. This suggests the Southwest region's VPD maxima are influenced not only by generally high temperature, but also large variability of actual vapor pressure. In addition, the Southwest U.S. shows the greatest linear trends in VPD.

While on average, actual vapor pressure is shown to increase from the south in the Eastern U.S. from Winter to Summer, Western U.S. vapor pressure only slightly increases in the lower-lying areas. The highest values of VPD by Seager et al.'s temporal average is approximately 4,700 Pa. Unfortunately, Seager et al. cut their investigation off sharply at the U.S. borderline. A full seasonal evolution of VPD into this region based on climatology prior to CMIP6 ScenarioMIP5-8.5 experiments, and during their first 10 years which have now passed in real time, are unknown., I say "into this region" as VPD appears to gain spatial extent from the Southern border of the U.S. in Seager et al., and possibly does so beginning further South from within Mexico.

In the current climatology, Mueller et al. (2020) quantified the probabilities of occurrence for varying fire extremities in the U.S. Southwest by VPD thresholds. Utilizing a hurdle model, Mueller et al. first found that increasing temperature and VPD as well as decreasing precipitation were associated with increasing regional area burned. Zhuang et al. (2021) have also shown that VPD is a meaningful proxy for wildfire risk in the Western US. Important to this study where I investigate VPD in a scenario where the highest level of greenhouse gas forcing is present (Meinshausen et al., 2020), Zhuang et al. investigated the anthropogenic and natural influences of VPD (as a wildfire proxy) for the period 1979 through 2020, given an increase in wildfire activity has occurred. They found that anthropogenic warming has contributed to at least twice as much as natural variability to increasing fire weather. While they completed case studies for prominent wildfires, they did not consider timing relative to precipitation with the NAM.

In terms of water vapor, there are discrepancies between observations and climate models (Simpson et al., 2023). Simpson et al. warn that observational increases of actual vapor pressure have not occurred with climatic increases in temperature, as is seen in CMIP6 climate models for the U.S Southwest. Drivers of potential model issue discrepancy are unknown. The key takeaway relevant to this study, analyzing VPD at a daily time scale, is that a global misrepresentation of the moisture transport response to warming may be present in the models.

3. Data and Methods

3.1. Vapor pressure deficit

Vapor pressure deficit is the difference between saturation vapor pressure and the actual vapor pressure of a parcel of air. The saturation vapor pressure (e_s) is defined as the partial pressure of the vapor in an air parcel if the parcel were saturated (i.e., if the dew point temperature were to reach the actual temperature), which increases approximately exponentially with the temperature of the parcel. Vapor pressure (e) is the partial pressure of the parcel of air by the actual vapor in the parcel. VPD can also be described as the saturated vapor pressure times one minus the relative humidity.

3.1.1. Vapor Pressure Deficit Formulations

VPD is given by Eqns. 1 and 2. In Eqn. 1, saturation vapor pressure is a function of temperature (T) and the actual vapor pressure is a function of dew point temperature (Td). In Eqn. 2, the actual vapor pressure is represented by relative humidity (RH; as a fraction) multiplied by saturation vapor pressure. Eqn. 2 is also commonly known as the saturated vapor pressure times one minus the relative humidity.

$$VPD = e_s(T) - e(T_d) \quad \textbf{(1)}$$

$$VPD = e_s(T) - e(e_s) * RH \quad \textbf{(2)}$$

Instead of using empirical tables such as The International Association for the Properties of Water and Steam reference dataset (Kretzschmar and Wagner, 2019), many have formulated analytical approximations for vapor pressure as a function of temperature, in which vapor pressure has an exponential relationship with temperature.

Murray (1967) formed an analytical solution for the saturation vapor pressure of liquid water that was considered acceptable for most meteorological purposes (Eqn. 3). The Murray approximation was accurate with a relative error of 10^-4 at T ~ > 0 °C, and 10^-5 at 50 °C, relative to the internationally accepted standard of the time, the Goff-Gratch (Goff and Gratch, 1946). Since Murray's formulation, several additional formulations have emerged, each with subtly different goals. Wexler and Hyland obtained empirical data for the saturation pressure of liquid water with respect to temperature, and formulated a lengthy analytical solution (Eqn. 4) accurate for temperatures between 0 °C and 100 °C. This equation was adopted by the American Society of Heating, Refrigerating, and Air-Conditioning Engineers, setting the then, new standard (Wexler, 1976; Hyland and Wexler, 1983). This equation is complex, warranting Bolton's (1980) analytically simple formulation (Eqn. 5), accurate between temperatures of -35 °C to 35 °C, and considered good for most meteorological applications with error on par to Wexler. Another commonly used approximation for saturated vapor pressure is the Improved Magnus solution (Alduchov and Eskridge, 1996), developed to meet the demands of upper air temperature regimes (defined as -80 °C to 50 °C, Eqn. 6).

$$e_s(T) = 6.1078 * \exp\left(\frac{17.2693882(T-273.16)}{T-35.86}\right) \quad \textbf{(3)}$$

$g_0 = -2.9912729 * 10^3$, $g_1 = -6.0170128 * 10^3$, $g_2 = 1.887643854 * 10^1$

$g_3 = -2.8354721 * 10^{-2}$, $g_4 = 1.7838301 * 10^{-5}$, $g_5 = -8.4150417 * 10^{-10}$,

$g_6 = 4.4412543 * 10^{-13}$, $g_7 = 2.858487 * 10^0$

$$e_s(T) = \sum_{i=0}^{6} g_i * T^{i-2} + g_7 * \ln(T) \quad \textbf{(4)}$$

$$e_s(T) = 6.112 * \exp\left(\frac{17.67*T}{T+243.5}\right) \quad \textbf{(5)}$$

$$e_s(T) = 6.1094 * \exp\left(\frac{17.625*T}{243.04+T}\right) \quad \textbf{(6)}$$

In Eqn. 3, T is in Kelvin (K) and es is in millibars (mb). In Eqn. 4, T is in Kelvin (K) and es is in Pascals (Pa). In Eqn. 5, T is in Celsius (°C) and es is in millibars (mb). In Eqn. 6, T is in Celsius (°C) and es is in Pascals (Pa).

Prominent papers describing VPD in my region of interest have used the above formulations, often citing earlier papers and mimicking methods for consistency. However, the region of interest experiences extremely hot temperature maxima, and is projected to get hotter on average, as I detail in Section 4. This region includes the location with the current global record for maximum temperature in modern recording history (Death Valley, 56.7 °C, World Meteorological Organization; Accessed 05/28/2025). The temperature regimes where VPD is expected to potentially be most extreme in this region are in temperature regimes where temperature is highest, due to the exponential dependence of saturated vapor pressure on temperature. Such temperatures in current climatology are often above 40 °C in the warm season (Adams and Comrie, 1997) with extremes above 50 °C. Some climate models have warmer base states than current climatology, projecting temperatures to rise even greater (described in more depth in Section 4). The analytical solutions of vapor pressure described above have non-negligible percent difference for temperatures greater than 50 °C (Figure 3.1.1). This region of climatological temperature and projected extremes requires appropriate approximations of vapor pressure.

Huang (2018) recognized the need for a vapor pressure formulation that was computationally simple and could be used with low relative error for areas that are projected to warm substantially, citing increases in projected heat waves (Coumou and Robinson 2013). Huang fit a least squares regression with five coefficients to minimize relative error of saturated vapor pressure from 0 °C through 100 °C (with a second equation from 0 °C to -100 °C; relative to The International Association for the Properties of Water and Steam reference dataset). Huang's fit was formulated from a physically representative, mathematically manipulated version of the Clausius-Clapeyron Equation. The Wexler solution does provide low relative error, on par with Huang, and the complexity of the Wexler solution is not of concern in this study, however the Huang equation still has a lower percent difference from the International Standard. Huang's equation is given in Eqn. 7, where T is in Celsius (°C) and es is in Pascals (Pa).

$$e_s(T) = \frac{\exp\left(34.494 - \frac{4924.99}{T+237.1}\right)}{(T+105)^{1.57}} \qquad \textbf{(7)}$$

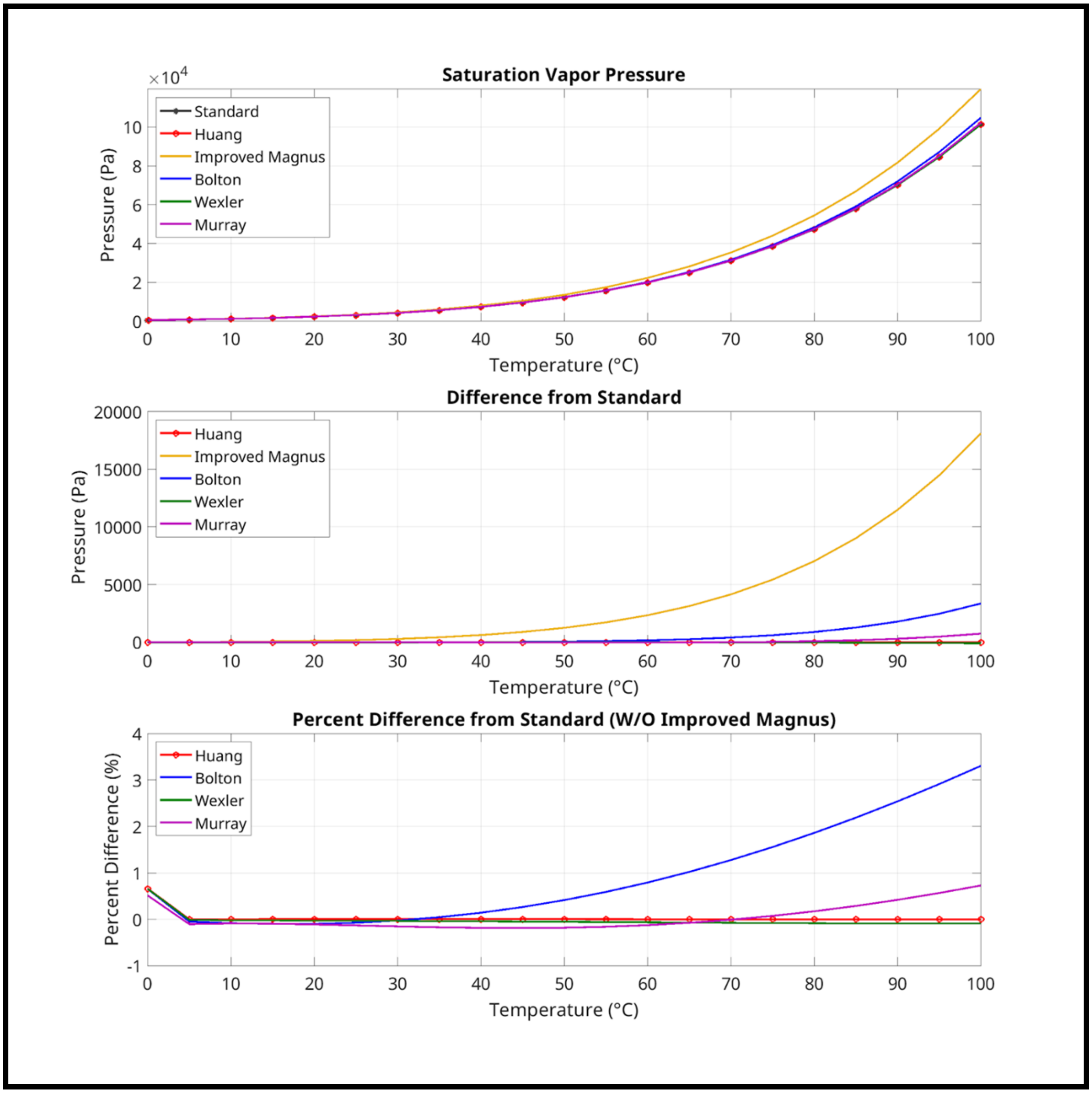

Figure 3.1.1. Vapor Pressure Methods. Top: Saturation vapor pressure in Pascals (Pa) with temperature in degrees Celsius (°C) for five different analytical methods (Huang, red; Improved Magnus, yellow; Bolton, blue; Wexler, green; Murray, purple) and The International Association for the Properties of Water and Steam reference dataset (Kretzschmar and Wagner, 2019) (Standard, black). Middle: The absolute difference of vapor pressure for five different analytical methods to The International Association for the Properties of Water and Steam reference dataset. Bottom: The percent difference of vapor pressure for four different analytical methods to The International Association for the Properties of Water and Steam reference dataset. The Improved Magnus method is not plotted as percent difference is much larger than the other four methods as temperature increases.

If a researcher wants to study VPD patterns of Southwestern wildfire extent through correlations, it is not critical that they use the same VPD formulation as used in this study (He et al., 2025). However, if a study wants to understand the extent of extremity for specific events, such as in case studies, then researchers should use the Huang (2018) formulation for vapor pressure deficit. There is an especial necessity for utilizing this method in regions where the temperature regime has extremities greater than 50 °C. Huang's formulations for saturation vapor pressure minimize relative error to The International Association for the Properties of Water and Steam reference dataset (Kretzschmar and Wagner, 2019) from -100 °C through 100 °C. Even if a study is considering average values of VPD (such as at a monthly time scale), researchers should still utilize Huang's formulation in calculating daily values to then average.

3.1.2. Time Averaging

Simply having an equation to approximate the saturated vapor pressure with temperature that has low relative error in the expected temperature regime of use is not solely sufficient. Also to consider are the type of temperature used and formulation for actual vapor pressure, varying the physical meaning of the obtained VPD. Saturation vapor pressure can be obtained by using the average, maximum, or minimum temperature for a given time range. Furthermore, the actual vapor pressure can be calculated by either using one of the solutions for saturated vapor pressure at the measured dew point temperature (average, maximum, or minimum; Eqn. 1), or can be calculated from the measured relative humidity (again, average, maximum, or minimum) with respect to the calculated saturation vapor pressure (Eqn. 2). Lastly, when calculating VPD on a monthly time scale, one can either average daily values for the entire month, or take an average value of temperature, etc…, for the entire month when calculating.

Of the methods for calculating VPD, irrespective of the approximation used for saturated vapor pressure, the formulation has impacts on the physical interpretation relative to VPD as a predictor of wildfires. He et al. (2025) have shown the influence of time averaging in VPD formulations, and their inferred relationships with wildfire area burned in the Western US. They found simply, that monthly calculations VPD are more accurate when calculated from daily data; monthly VPD calculated from daily data provides a higher correlation to wildfire area burned. However, the type of temperature used (average, maximum, or minimum) has little effect on correlations to wildfires. He et al. warn that in a future changing climate that changing diurnal temperature cycles may cause important divergences between different methods of calculating VPD.

3.1.3. Vapor Pressure Deficit (as used)

In this study VPD is calculated from Equation 2, using Huang's equation for es, where T is the maximum daily temperature. Maximum daily temperature is used here, to calculate VPD physically interpreted as the maximum daily VPD at each daily time step. Given here again, in this equation relative humidity and saturated vapor pressure are used to calculate vapor pressure. The decision to use this method is due to data availability, where relative humidity is a model output variable and dew point temperature is not. Units for VPD are Pascals (Pa). A simplified version of the equation used for VPD in this study is given in Eqn. 8, where T is the maximum temperature in Celsius (°C) and RH is the relative humidity as a fraction.

$$\mathrm{VPD} = \frac{\exp\left(34.494 - \frac{4924.99}{T+237.1}\right)}{(T+105)^{1.57}}(1 - RH) \tag{8}$$

When Monthly VPD is used in this study, monthly VPD is calculated by averaging daily calculated VPD using Eqn. 8, at every grid cell for the month. As stated prior, this method of using daily values of VPD to get an average monthly VPD is more accurate than averaging monthly values to get a monthly VPD (He et al., 2025).

3.2. CMIP6 models

The nine climate models used in this study are listed in Table 3.2 with corresponding country of origin and resolution. There are two models from the same Canadian modelling family, two models from the same Russian modelling family, one French model, one Korean model, one Japanese model, and two models from the same German modelling family. The two Canadian models (CanESM5-1 & CanESM5) are at the same resolution (128x64; 2.8°x2.8°), and the lowest resolution models used in this study. While resolution of some models may be lower than others, it does not suggest a more accurate nor inaccurate projection into the future. A finer resolution can, however, provide better representation of atmospheric and oceanic processes (Iles et al., 2020; Navarro-Racines et al., 2020; Moreno-Chamarro et al., 2022; You and Ting, 2023). The highest resolution model used in this study is the MPI-ESM1-2-HR model (384x192; 0.9°x0.9°).

Table 3.2. Names, country of origin, and resolution of nine climate models.

Model	Country	Resolution
CanESM5-1	Canada	2.8°x2.8°
CanESM5	Canada	2.8°x2.8°
INM-CM4-8	Russia	2°x1.5°
INM-CM5-0	Russia	2°x1.5°
IPSL-CM6A-LR	France	2.5°x1.3°
KACE-1-0-G	Korea	1.9°x1.3°
MIROC6	Japan	1.4°x1.4°
MPI-ESM1-2-HR	Germany	0.9°x0.9°
MPI-ESM1-2-LR	Germany	1.9°x1.9°

Only one variant from each model was used in this study, all being variant r1i1p1f1. Five models used were on their native grid ("gn"), while the French and Korean models were regridded to the data provider's preferred target grid ("gr"), and the two Russian models were regridded to a grid other than the native grid and other than the preferred target grid ("gr1") (Taylor et al., 2018; Accessed from https://github.com/WCRP-CMIP/CMIP6_CVs/blob/main/CMIP6_grid_label.json on 06/09/2025). Data was made available and downloaded from the Earth System Grid Federation (Accessed from https://esgf-node.ornl.gov/search on 06/09/2025).

3.2.1. Region Averaging and Landmask

Besides knowledge of VPD in the general Southwest U.S. and Northern Mexico, considerations based upon the grid resolutions of each model were necessary to reduce bias on region averaging. With the exception of the two Canadian models, all the models are at different resolutions. When setting longitude and latitude bounds for this region, the actual bounds for each model are for grid cells that have a coordinate closest to the bounds. Given that the highest resolution model is sufficiently higher than the lowest resolution model, if one is not careful, a bias in any average variable for this region could be introduced.

The longitude and latitude bounds for my region of interest are defined as: 93° to 123° west and 22° to 42° north. This boundary allowed for capture of VPD from the West Coast U.S. to the Gulf of Mexico through the Northern extent of the Mexican coastline. This boundary captures the general area of the North American Monsoon (Adams and Comrie, 1997), the broad extent of the VPD maximum shown in previous studies (Seager et al., 2015), and the general extent of VPD maximum seen in this study. This boundary also well accommodates the resolutions of all models used, and can be seen best in Figure 3.2.1 displaying the landmasks for this region.

The exact scheme used to define this region is as follows. Knowing the amount of latitude and longitude increments in each model, I multiplied this amount by the intended boundary coordinates (as fractions of the total degrees in the globe's coordinate system), and rounded this value to the nearest whole number. The product is the index for the respective model, corresponding to the grid cell with the nearest boundary coordinates as the predefined "box."

To apply landmasks to this region, I set every grid cell that was neither in this region, nor given as 100% land (defined in the respective model landmask files) as NaN, and omitted NaNs whenever averaging for the box. Landmasks are plotted in Figure 3.2.1, for grid cells given as 100% land. Each modelling group defines land placement differently, and uses different landmasking schemes. Some modelling groups provide landmask files as a gridded value of 1 or 0 to specify land versus ocean, while others provide percentages and increments of their choosing to specify a percentage of land in each grid cell. Landmasks define non-land, being ocean, as simply ocean; The definition of land in landmasks includes ice-shelves, lakes and rivers. CMIP6 landmasks have the variable id: "sftlf."

Note that MPI-ESM1-2-HR is the model which includes a distinct ocean in the Gulf of California and land in the Baja California peninsula. Also note that some applied landmasks do not include California's Central Valley, nor low-lying coastal regions in Mexico.

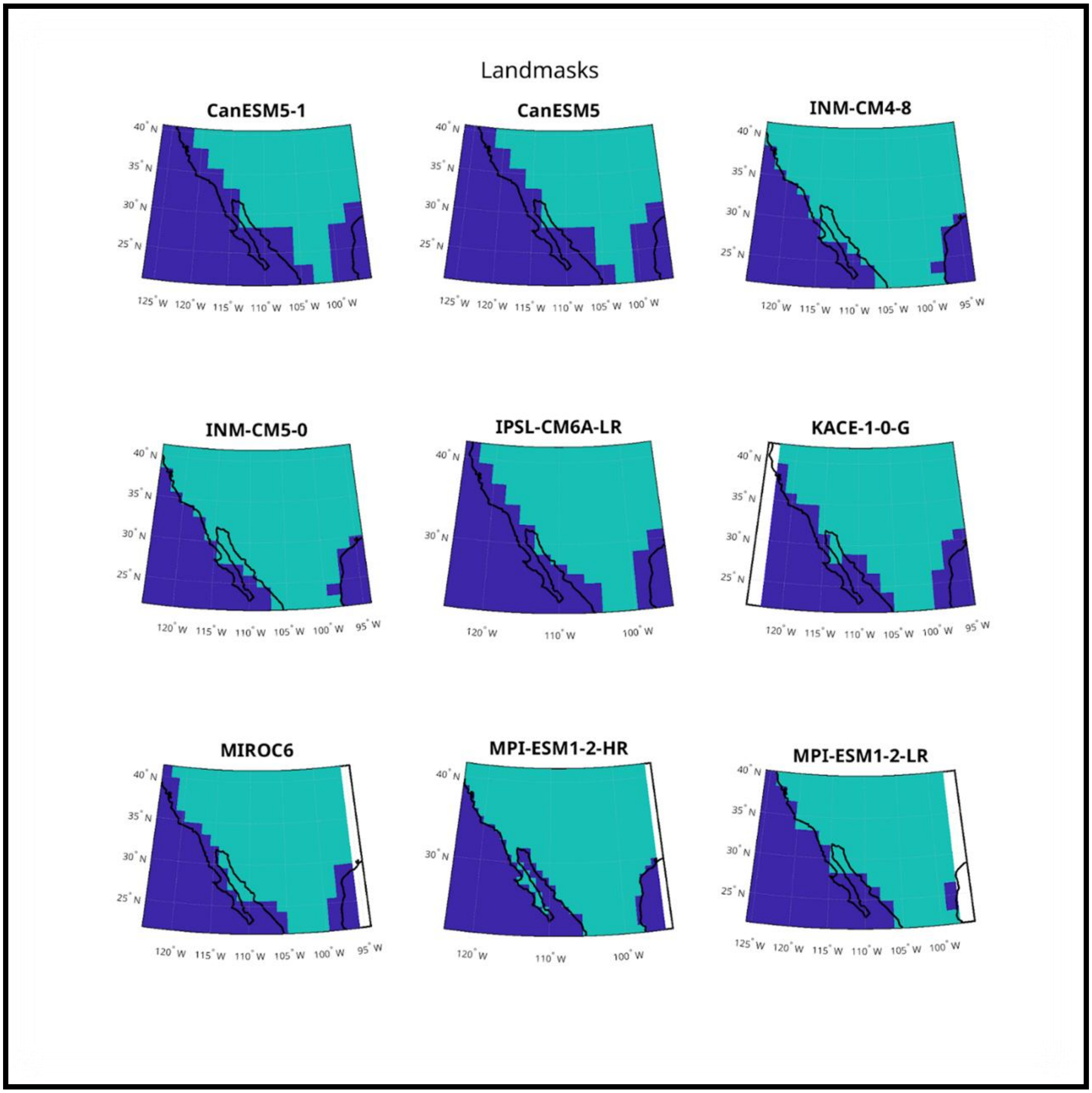

Figure 3.2.1. Landmasks. Plotted in color are grid cells within the region of interest. Landmasks, in teal, are defined by each respective model as grid cells with a percentage of land equal to 100%. Grid cells in blue have a landmask percentage less than 100%, and contain some proportion of land. In black are coastlines. The region is limited to the region of interest, following methods described in Section 3.2.1.

The landmask for the KACE-1-0-G model was not available. The landmask for the ACCESS-CM2 and ACCESS-ESM1-5 models were used instead, as these models had the same resolutions (with an important note to the winds). As the cutoff for land percentage used in this study is 100%, suspected error introduced here is only to unknown definitions of land placement by each modelling group, and only an issue for select grid cells (likely around the Gulf of California) that may have been (but also may not have been) inadvertently used when defined by ocean by the KACE-1-0-G modellers. KACE-1-0-G has a unique grid scheme for the wind components (unique to the other models used in this study), in that the resolution of the model is 192x144 for every variable except the meridional wind component, being 192x145. The ACCESS modelling group follows this same idea, and the ACCESS-CM2 landmask is applied to all KACE-1-0-G variables, except the meridional wind component, of which the ACCESS-ESM1-5 landmask is applied to. Prior to the use of ACCESS landmasks, I verified consistent grid cell boundaries between models.

When averaging models in this region, a landmask is always applied. Furthermore, a latitude weighting is also applied due to uneven grid cell sizes as a function of latitude. To apply a latitude weight, I multiply the grid cells by a normalization factor (function of latitude) to the respective grid cells at each latitude. This ensures equal weighting of each grid cell value in the overall box average.

Sometimes models are compared based on a time series average in the boxed region of interest. Due to differing dating schemes, this is sometimes presented as a fraction of days of the year instead of by the actual day of the year. Models used that observe leap years include: IPSL-CM6A-LR, MIROC6, MPI-ESM1-2-HR, MPI-ESM1-2-LR, models with constant 365-day years include: CanESM5-1, CanESM5, INM-CM5-0, INM-CM4-8, and models with constant 30-day months (360-day years) include: KACE-1-0-G.

3.2.2. CMIP6 Meteorological Variables

The meteorological variables from direct CMIP6 model outputs used in this study are given in Table 3.2.2 alongside their CMIP6 variable id and native units, with alternatively used units in parenthesis. Data is complete from years 2015 through 2100. Precipitation flux density is converted to a daily average precipitation value for the respective grid cell by multiplying the given value by 86400 seconds/day.

Table 3.2.2. Meteorological variables, corresponding CMIP6 variable id and units, and units used in this study.

Variable Name	Variable ID	Units (Units Used)
Temperature	tas	K
Maximum Temperature	tasmax	K
Minimum Temperature	tasmin	K
Precipitation Flux Density	pr	mm/m^2*s (mm)
Sea Level Pressure	psl	Pa
Latent Heat Flux	hfls	W/m^2
Relative Humidity	hurs	% (fraction)

3.3. Maps

Maps used in this study were created in MATLAB, using MATLAB's Mapping Toolbox. The function geoshow() provided a map projection that was best fit to preserve the size and shape of features in the area of interest. All maps are bound by the region 0° N to 80° N and 50° W to 180° W (using the same methods described in Section 3.2.1 for differing model resolutions). Functions used to plot isolines include contourm() and contourfm(), where the "m" stands for being part of the Mapping Toolbox, and the latter applying a fill between isolines. The acknowledgement of these methods is important, as to create isolines, the gridded behavior of model outputs are disguised. Artifacts of the spatial plotting methods are undeniably present.

4. Analysis and Discussion of Results

4.1. Introduction

This section is dedicated to describing model climatology. Establishing an initial model climatology provides important context in understanding changes within and between models as each model has a different base state. The Southwest U.S. and Northern Mexico region is compared between models by the first 20 and last 20 years spatially, as well as through region average time series. In addition, VPD extremes in each model are defined here, described here, and compared here. This section provides important insight to model discrepancies on extreme VPD events. Differences between model projections and expected features (based on current climatology) are also discussed in this section.

4.2. Extreme Vapor Pressure Deficit Events

Extreme VPD events are defined as the three highest average VPD values in the landmasked Southwest U.S. and Northern Mexico region, where the year of an event for each model is unique. The INM-CM5-0 had its second extreme event (9470 Pa) just 51 days before its most extreme event, and was replaced on the extreme events table (Table 4.2) with the next highest VPD value. Models had their extreme events between the dates of 02/24 and 08/02. Of the 27 events, one took place in February, three in March, three in April, ten in May, three in June, four in July, and one in August. Most of the 27 events took place in the year 2090 or later (17 events). Eight events happened between the years 2079 and 2090. Two relatively early events took place; MPI-ESM1-2-HR had its third event in 2062, and INM-CM5-0 had its third event in 2055.

In regard to time of year, the three MPI-ESM1-2-LR events were the earliest events of all 27 events. The MPI-ESM1-2-HR events were also early, being in late April and early May. MIROC6 events were in mid-April through early May. In contrast, the two Russian and Korean models had their extreme events take place later in the year. INM-CM5-0 had two of the latest events, with its earliest in mid-July.

Table 4.2. Extreme VPD dates and values.

Model	Date; 1st Extreme	VPD; 1st Extreme	Date; 2nd Extreme	VPD; 2nd Extreme	Date; 3rd Extreme	VPD; 3rd Extreme
CanESM5-1	5/21/2095	11089 Pa	5/13/2093	9935 Pa	6/3/2084	9793 Pa
CanESM5	5/10/2096	11450 Pa	5/18/2090	10618 Pa	5/19/2099	10275 Pa
INM-CM4-8	6/26/2089	10564 Pa	5/29/2099	10439 Pa	7/14/2087	10135 Pa
INM-CM5-0	7/23/2095	9695 Pa	8/2/2097	9396 Pa	7/14/2055	9121 Pa
IPSL-CM6A-LR	3/24/2096	6687 Pa	5/5/2094	6395 Pa	4/9/2086	6321 Pa
KACE-1-0-G	7/20/2100	12610 Pa	6/1/2091	10356 Pa	5/27/2099	10093 Pa
MIROC6	4/19/2090	20199 Pa	5/8/2081	18486 Pa	4/18/2086	17194 Pa
MPI-ESM1-2-HR	4/17/2099	7046 Pa	5/4/2080	6880 Pa	4/25/2062	6701 Pa
MPI-ESM1-2-LR	3/27/2079	6777 Pa	2/24/2096	6680 Pa	3/22/2099	6677 Pa

Spatially, the 27 extreme VPD events almost all have their area of maximum VPD contained within the latitude and longitude limits for the region of interest, as defined for this study (outlined in red in figures 4.2.1-3). Exceptions to this are in the 1st extreme event in the KACE-1-0-G model, having a broad region of maximum VPD spread along the Great Plains and centered on the Eastern edge of the region, and the 2nd extreme in the INM-CM5-0 model where a region of maximum VPD is similarly spread across the Great Plains.

While each model has its own subtleties, there is general agreement in two regions of maximum VPD that develop within this broader region of interest. One region of high VPD tends to form in Southern California, with a coastal border, stemming Northward from the upper Northwestern edge of the Sonoran Desert. The second region is to the East of the broader region of interest, sprawling more broadly through the Great Plains and the Eastern part of the Chihuahuan desert. The sprawling nature varies between models and extremes. High VPD (but not usually the highest) tends to spread across the general Arizona and New Mexico area connecting the two regions of maximum VPD. There is not enough information with merely three events from each model to determine if seasonality contributes to the spatial extent of events. The MIROC6 model shows the highest VPD of all nine models, with VPD greater than 20,000 Pa in all three cases. No other model has VPD greater than 17,000 Pa, and most are several thousand Pascals less.

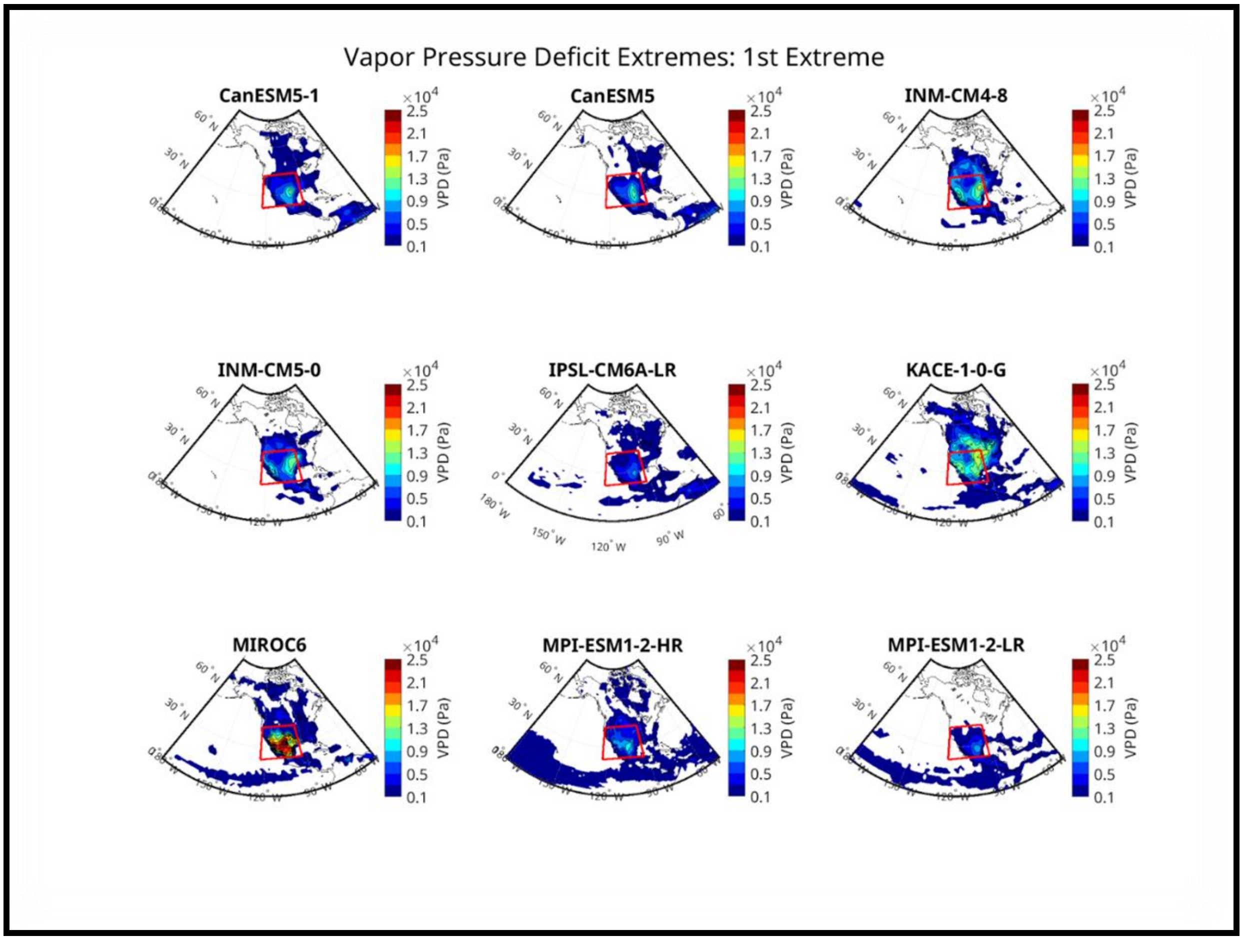

Figure 4.2.1. Vapor Pressure Deficit Extremes: 1st Extreme. Spatial extent of the most extreme case of region averaged VPD, plotted as color filled contours for North America. The Southwest U.S. and Northern Mexico region of interest is outlined in red. VPD less than 1,000 Pa is not plotted, in order to provide maximum contouring over the land region of interest.

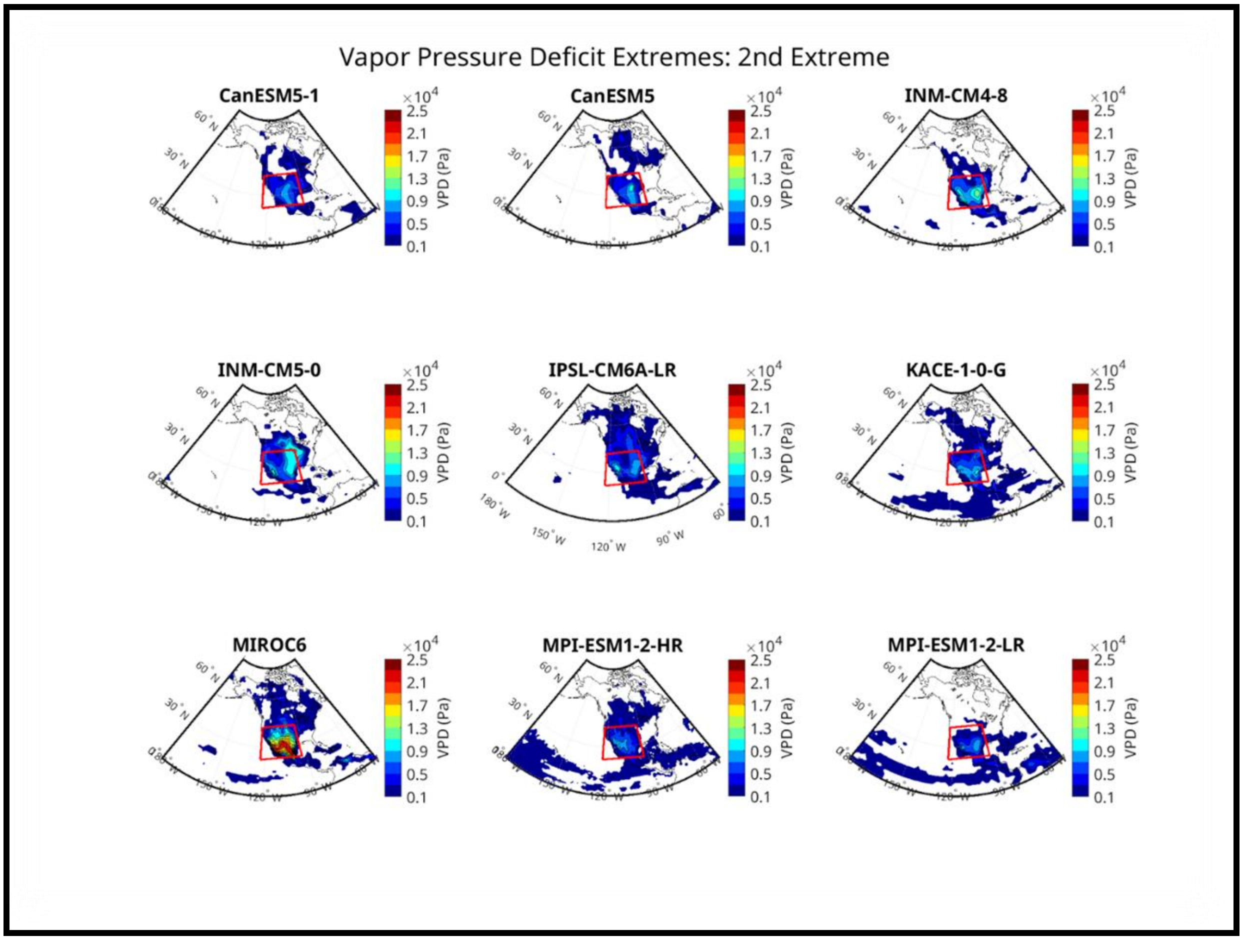

Figure 4.2.2. Vapor Pressure Deficit Extremes: 2nd Extreme. Same as in Figure 4.2.1, except for the 2nd most extreme case of VPD.

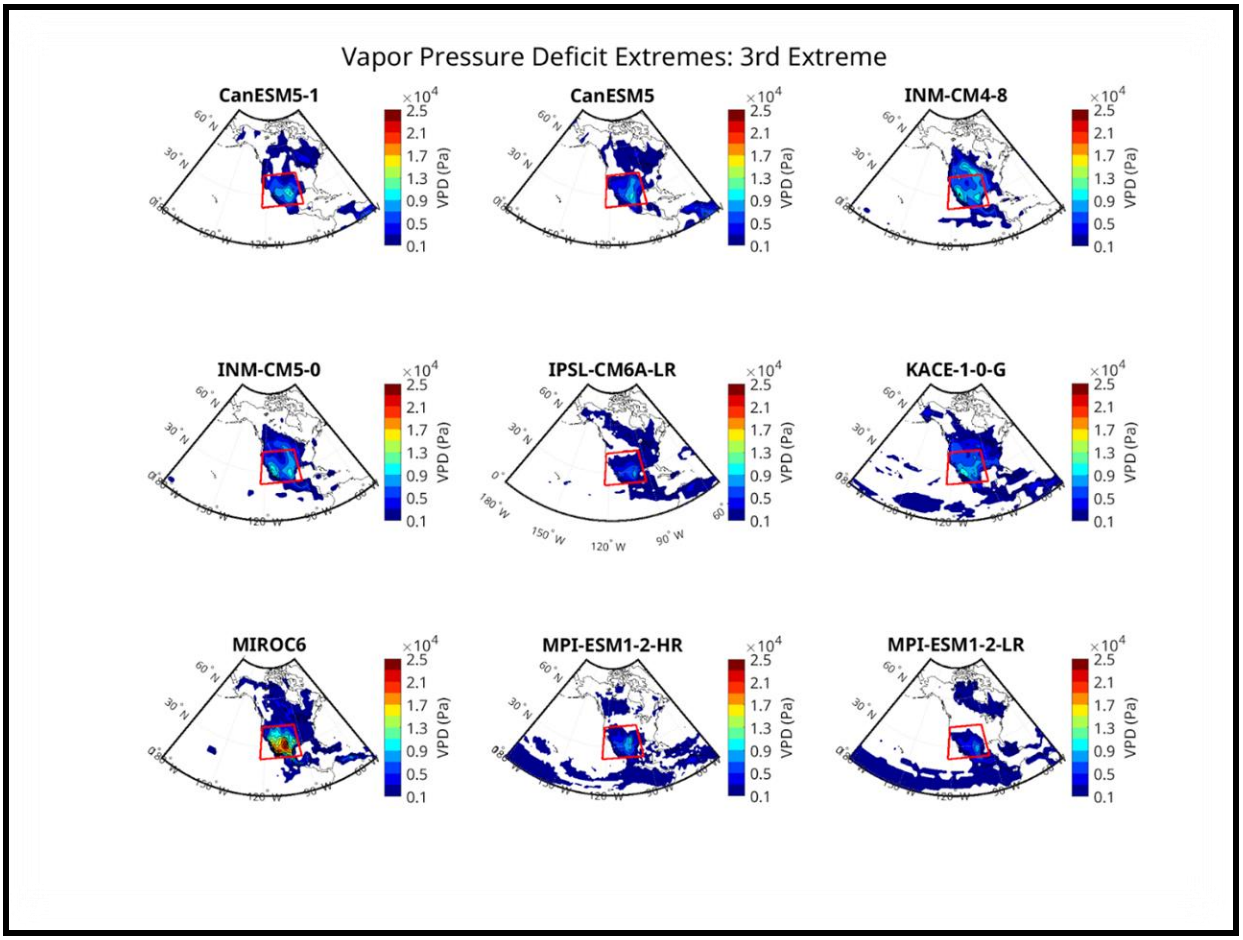

Figure 4.2.3. Vapor Pressure Deficit Extremes: 3rd Extreme. Same as in Figure 4.2.1, except for the 3rd most extreme case of VPD.

4.3. Geographical Climatology

With the warmest in MIROC6, all nine models show two areas of highest maximum temperature in their first 20 years (Figure 4.3.1). These are, in the Gulf of California and the Sonoran Desert surrounding it, and in the lower part of the General Great Plains opposite the Sierra Madre Occidental and primarily in coastal Southern Texas. Similar to the spatial extent of variability seen in Seager et al. (2015), RH is at a strong minimum to the west with RH values between 20% and 40%. Seager et al. did not show the spatial extent of RH (rather vapor pressure), however when taking into consideration the temperature patterns in Figure 4.3.1, it is clear to say (in general) that actual vapor pressure is lower on the west side of my region. Furthermore, the two observed areas of maximum VPD have different influences of vapor pressure in their first 20 years that result in different VPD maxima behavior.

Patterns for the first 20-year average VPD (Figure 4.3.4) align well with the spatial extent of the extreme VPD events, except in that the extreme VPD events tend to have a broader extent to the north-northeast from the eastern maxima. The extreme events also have warmer average temperatures (Section 4.4, spatial extent not displayed). The first 20-year average spatial extent for VPD in the KACE-1-0-G model shows a very similar VPD sprawl across the Eastern U.S. as is seen in its most extreme event. The KACE-1-0-G model has somewhat later extremities than other models, with its most extreme being the second latest of all 27 events (later means warmer climatologically), displaying (in one instance) how VPD in the eastern part of my region is influenced primarily by temperature.

Being comprised of significant deserts, it is no surprise that the entire region has limited precipitation in the first 20-year average (Figure 4.3.3). Precipitation is however on average slightly less off the California coast and in the Sonoran Desert than on the east side of the region of interest. Changes in maximum temperature, RH, and precipitation into the last 20 years of the model runs display little bias towards either VPD maxima areas (not displayed). In Figure 4.3.5, changes in VPD do show bias, likely due to their already warm first 20-year temperatures combined with the exponential behavior of VPD. Changes in temperature at higher temperatures results in greater changes in VPD.

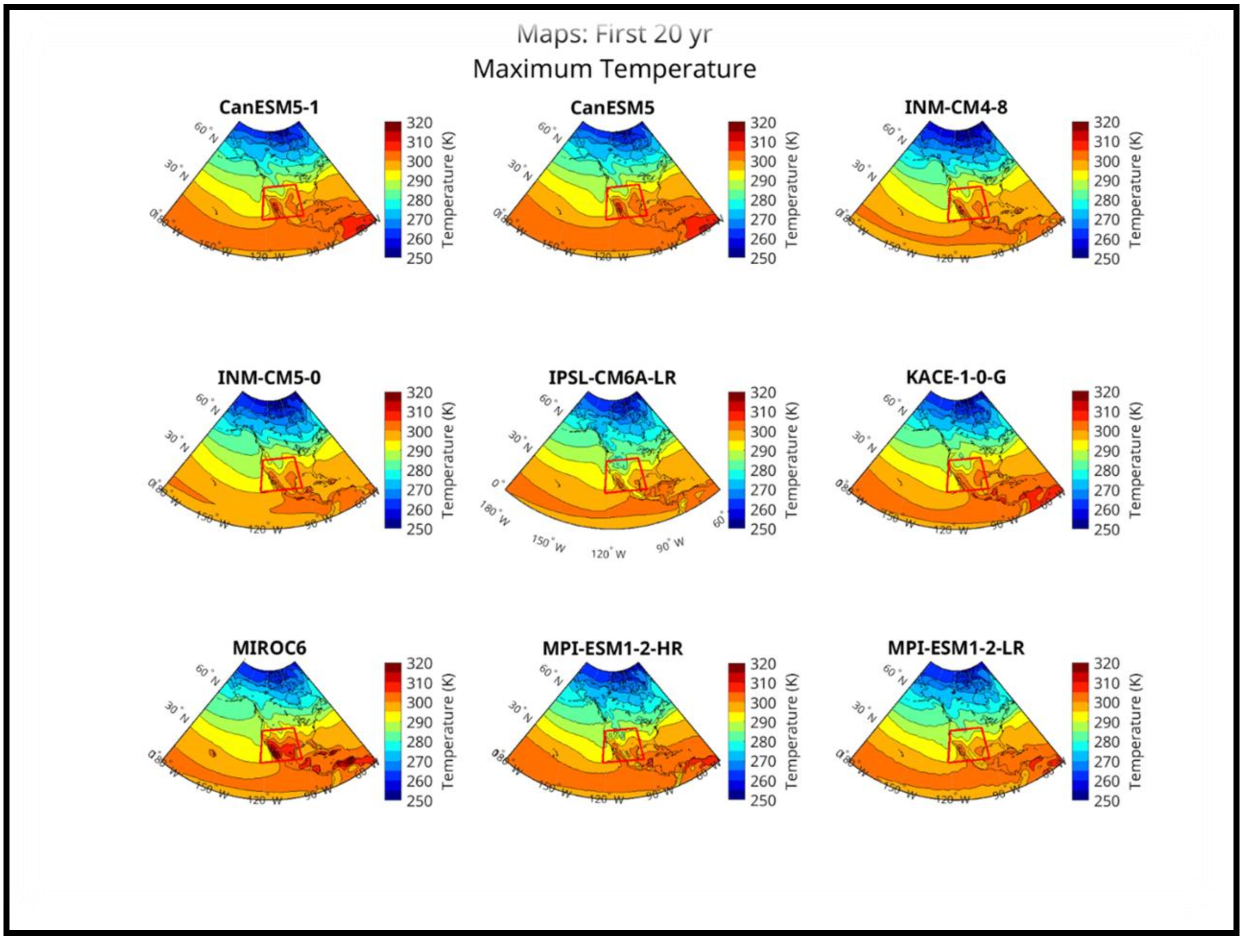

Figure 4.3.1. Maps: First 20 yr; Maximum Temperature. Average maximum temperature for the first 20 years of all nine models, plotted as color filled contours for North America. The Southwest U.S. and Northern Mexico region of interest is outlined in red.

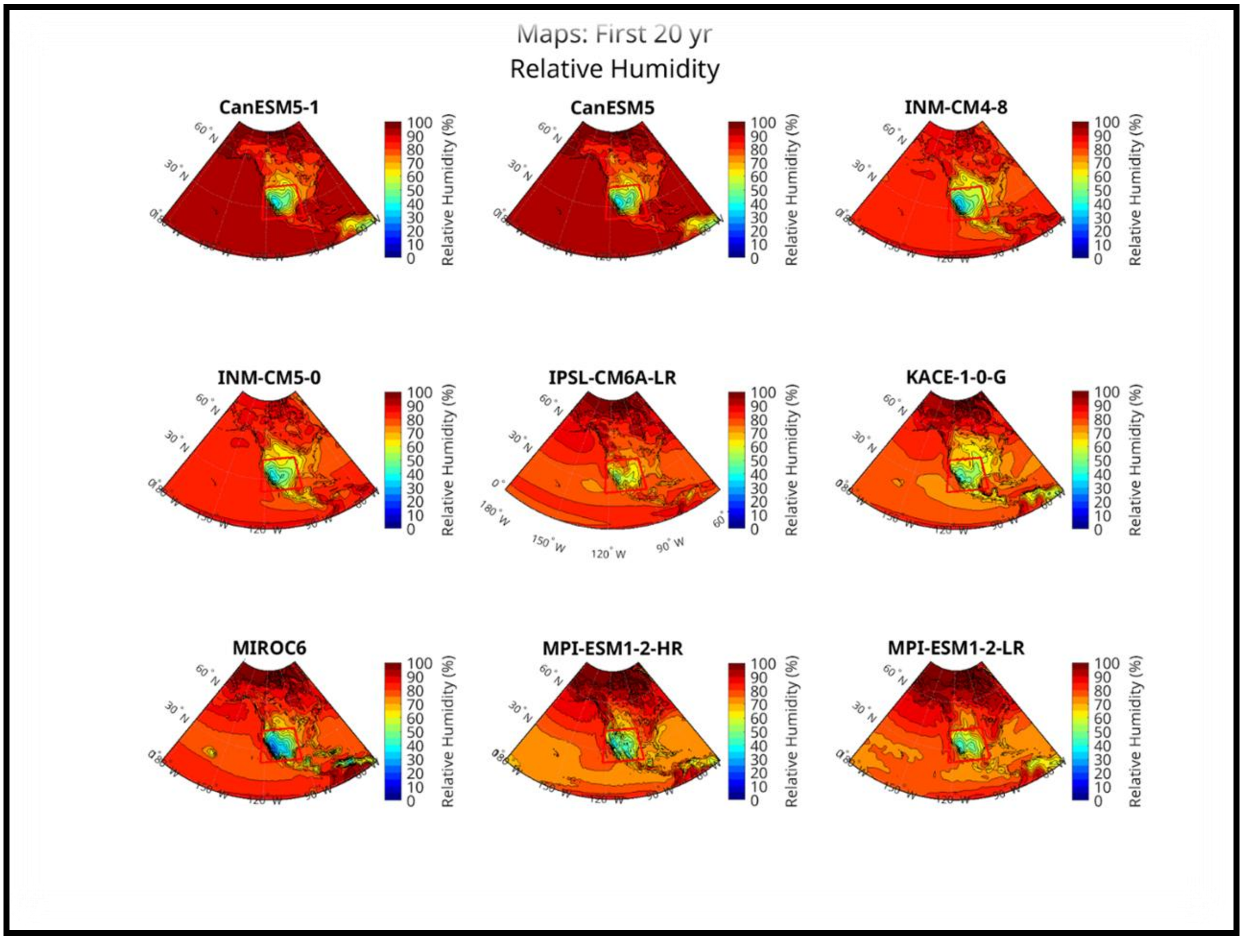

Figure 4.3.2. Maps: First 20 yr; Relative Humidity. Same as in Figure 4.3.1, except for Relative Humidity.

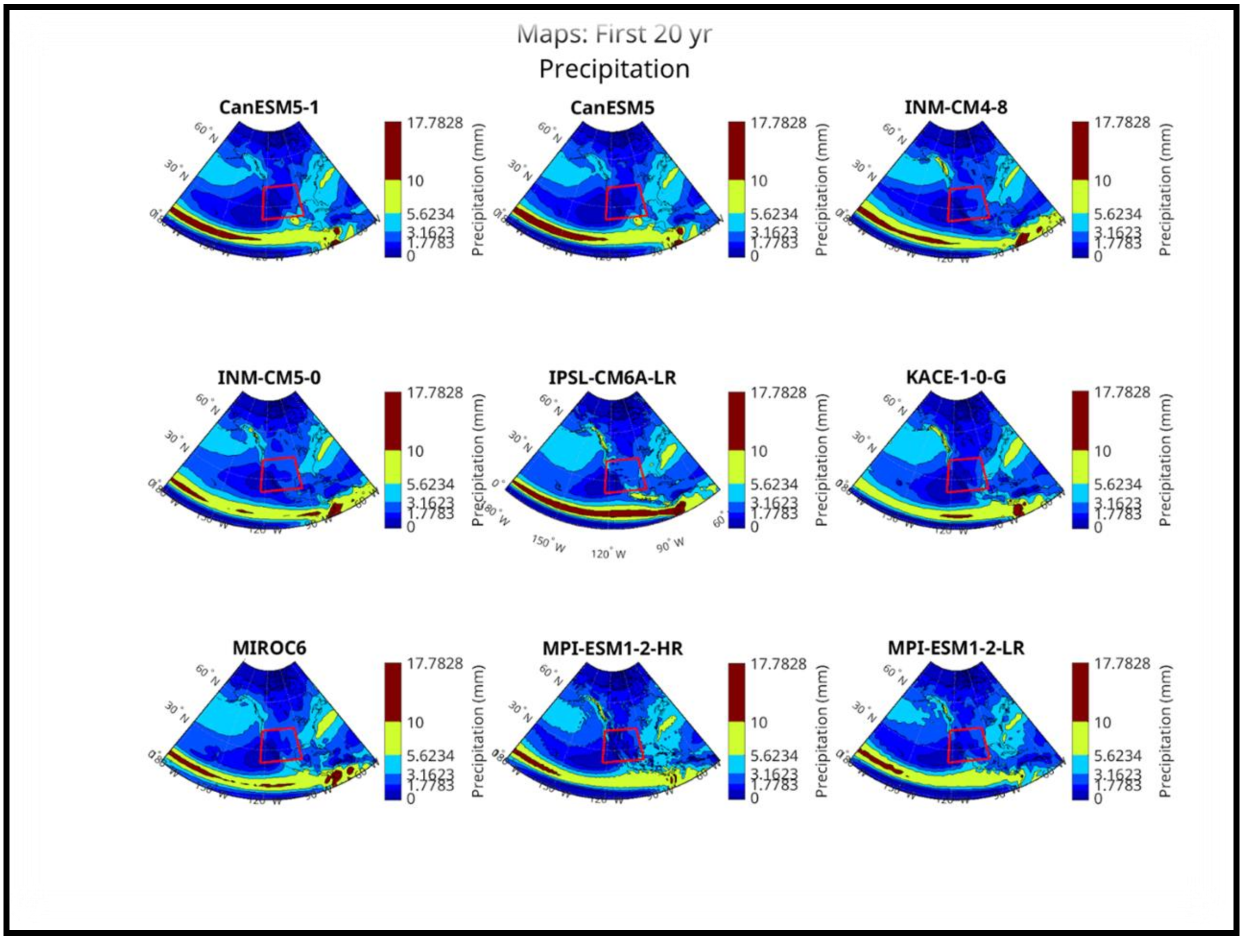

Figure 4.3.3. Maps: First 20 yr; Precipitation. Same as in Figure 4.3.1, except for Precipitation.

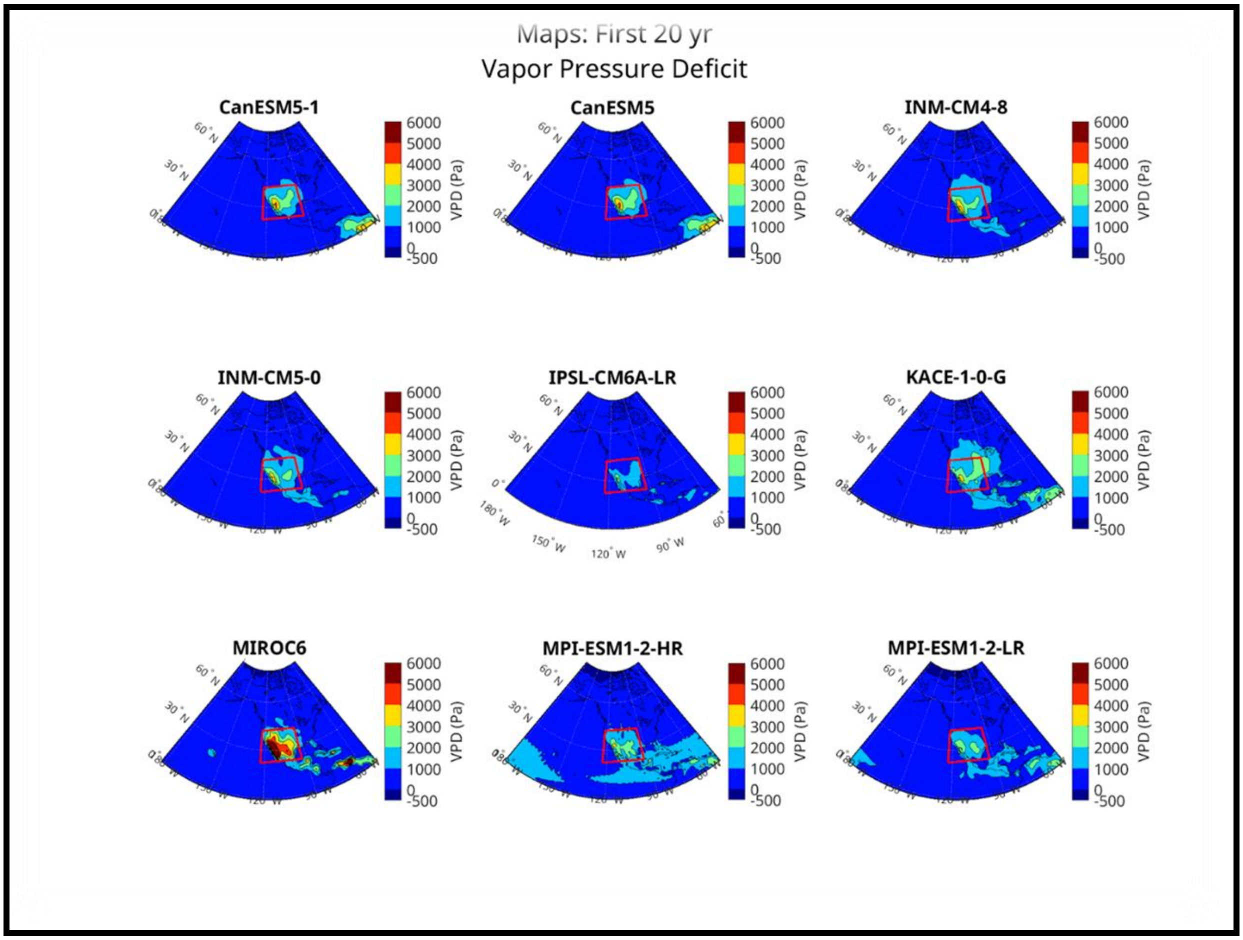

Figure 4.3.4. Maps: First 20 yr; Vapor Pressure Deficit. Same as in Figure 4.3.1, except for Vapor Pressure Deficit.

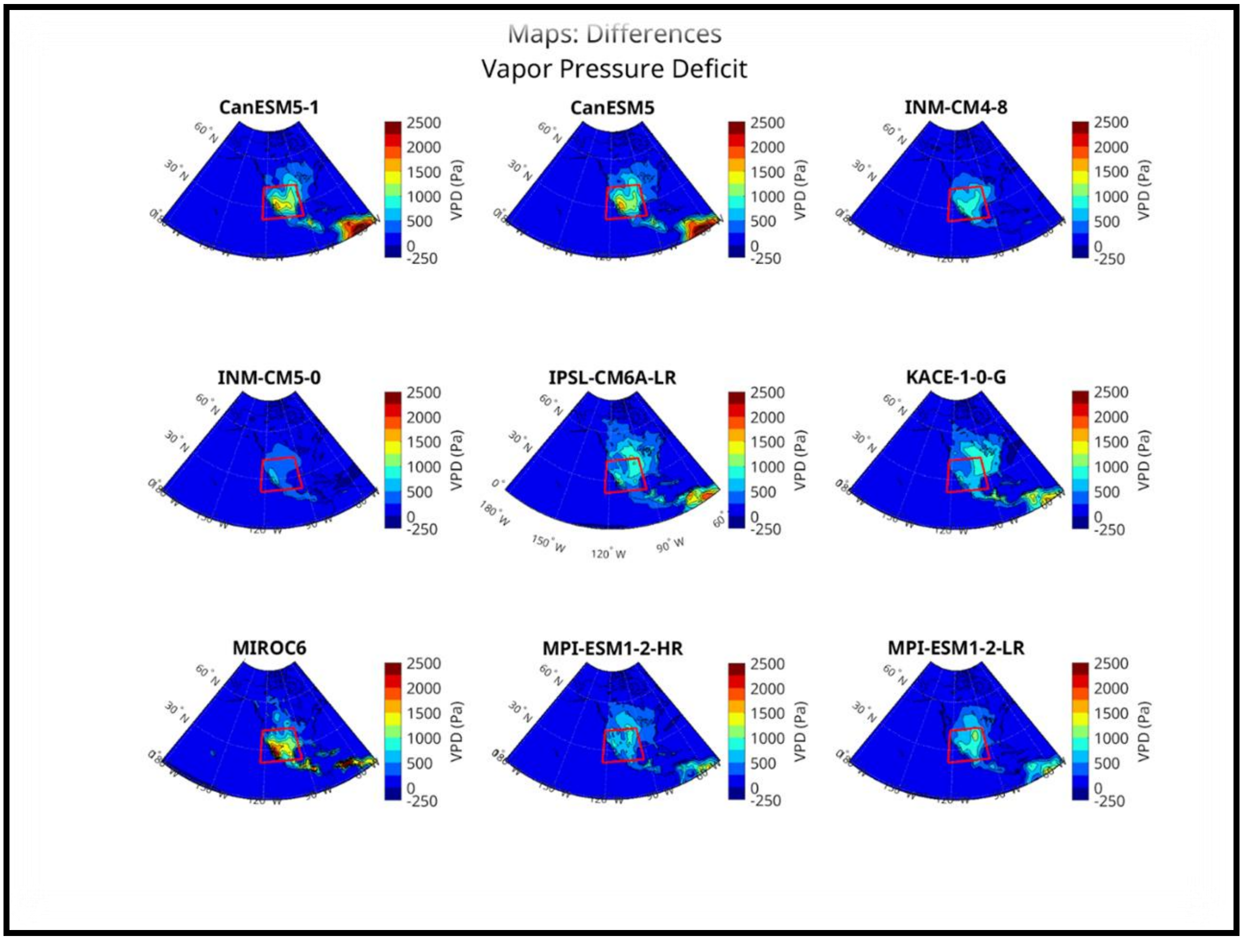

Figure 4.3.5. Maps: Differences; Vapor Pressure Deficit. Same as in Figure 4.3.4, except with the difference between the last 20 year averages (2080-2100) and first 20 year averages (2015-2035) plotted instead.

4.4. Model Climatology

This section is similar to the previous section on geographical climatology, individually covering model base states with comparisons between models. Additionally, changes of models in the last 20 years of model runs are compared to their first 20 years. These descriptions are used to explain the timing and behavior of the extreme VPD cases, described in detail by event within each respective model subsection below.

At the beginning of this section are four figures with time series. The first two figures display an average time series of the first 20 years (years 2015 through 2035) within each model (models split between the figures), with an ensemble average in black. The ensemble average is an average of all nine models displayed. The time series is on a x-axis of fraction of year, with years interpolated to 365 days in order to compare them (as models do not have consistent days every year). The next two figures are in the same format, displaying the difference between the last 20 years to the first 20 years of the model run (years 2080 through 2100 minus 2015 through 2035). These figures are discussed in the respective model subsections below.

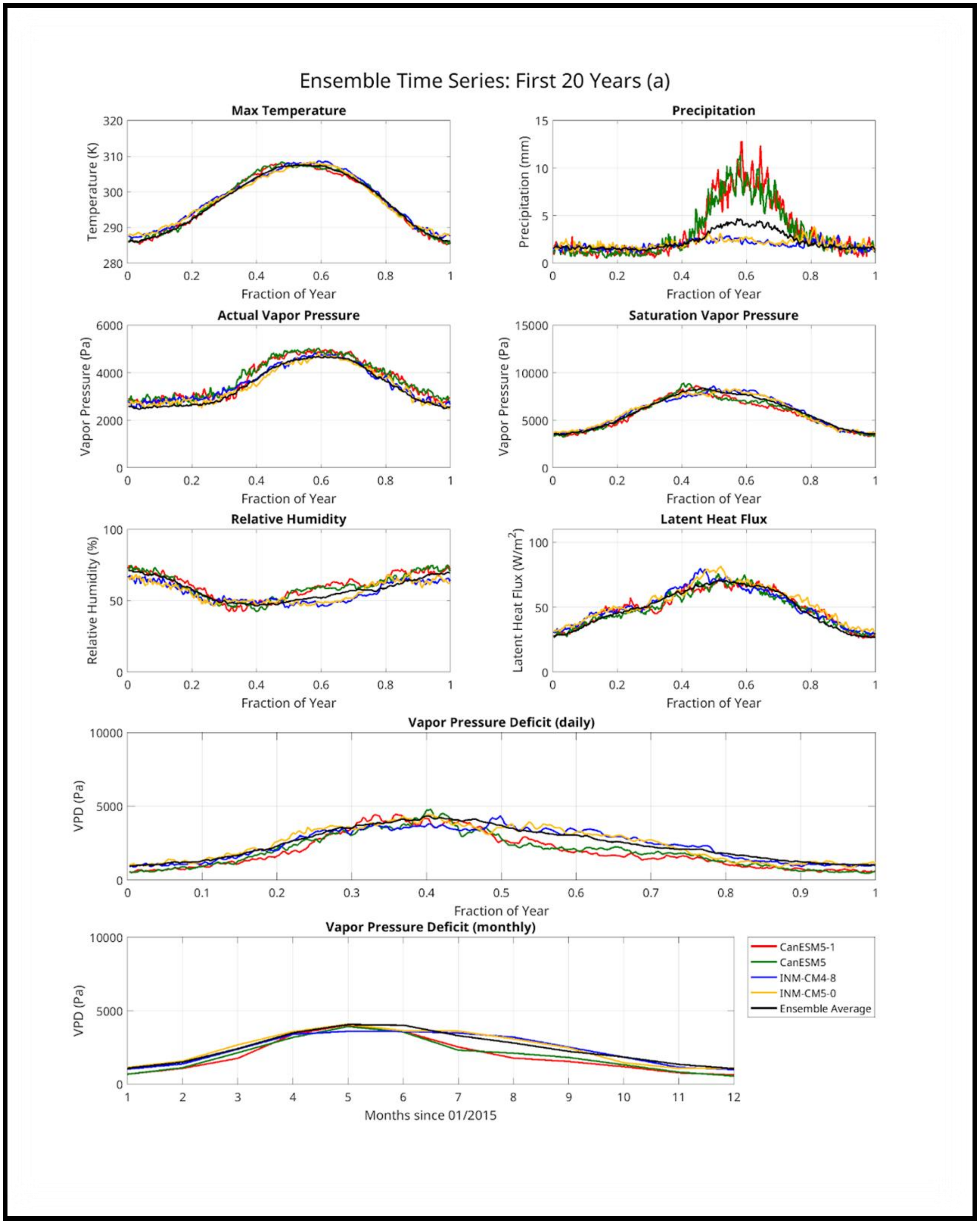

Figure 4.4.1. Ensemble Time Series: First 20 Years (a). Yearly average time series for select variables of the first 20 years (2015-2035) for each model run, plotted by fraction of year. Four out of nine models are in color. Ensemble average of all nine models is in black.

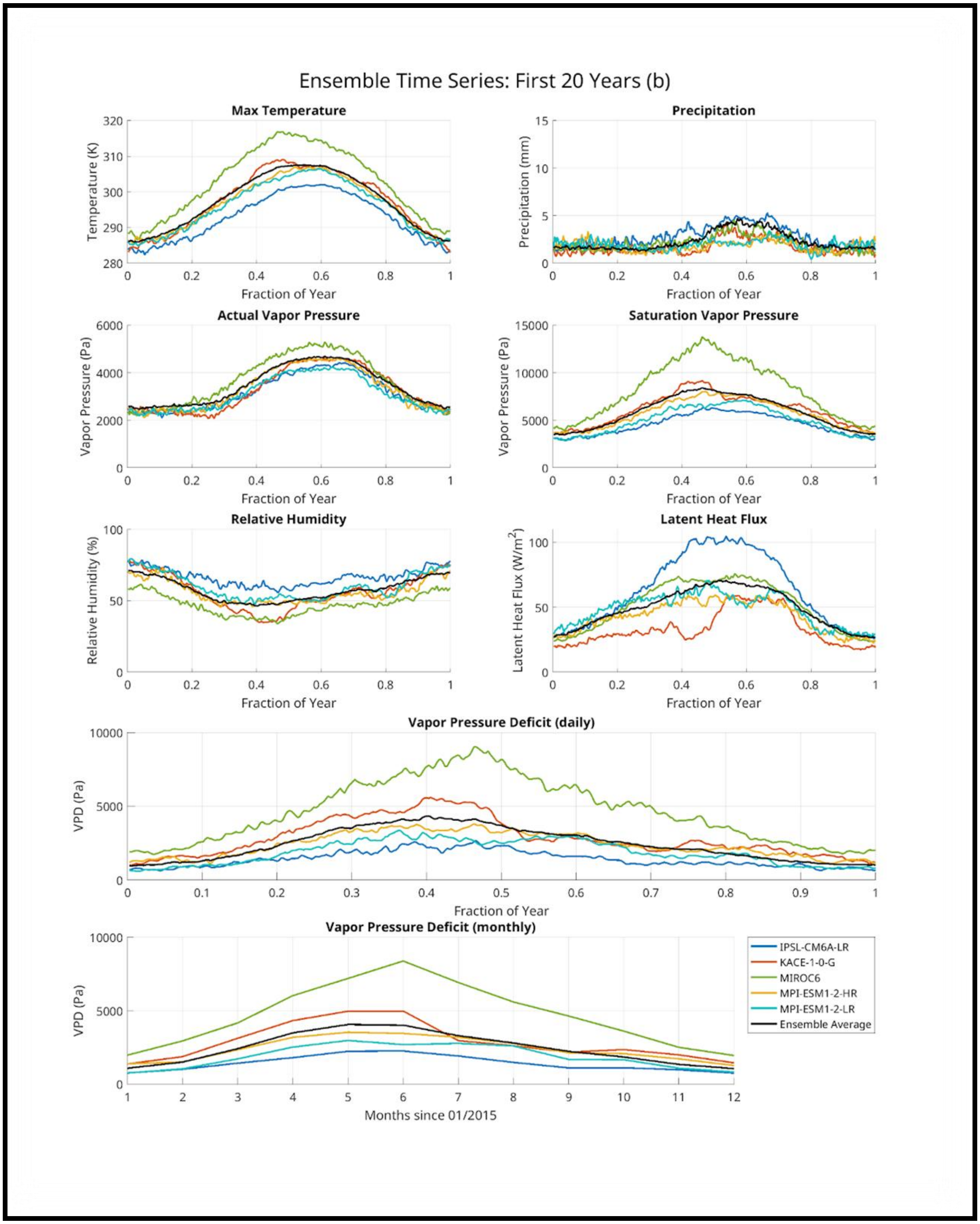

Figure 4.4.2. Ensemble Time Series: First 20 Years (b). Same as in Figure 4.4.1, except with the remaining five models plotted in color, instead.

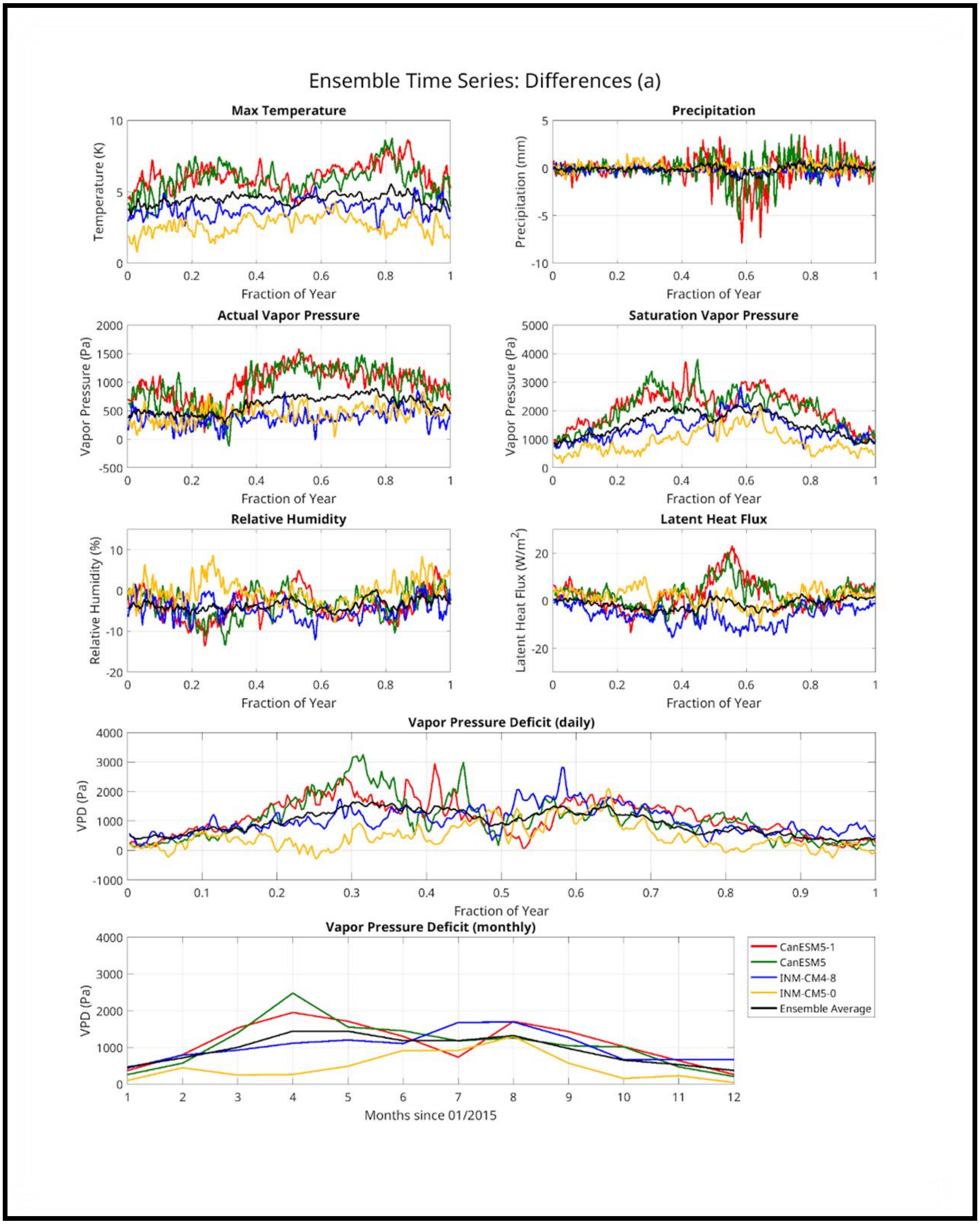

Figure 4.4.3. Ensemble Time Series: Differences (a). Same as in Figure 4.4.1, except with the difference from the last 20 year averages (2080-2100) and first 20 year averages (2015-2035) plotted instead.

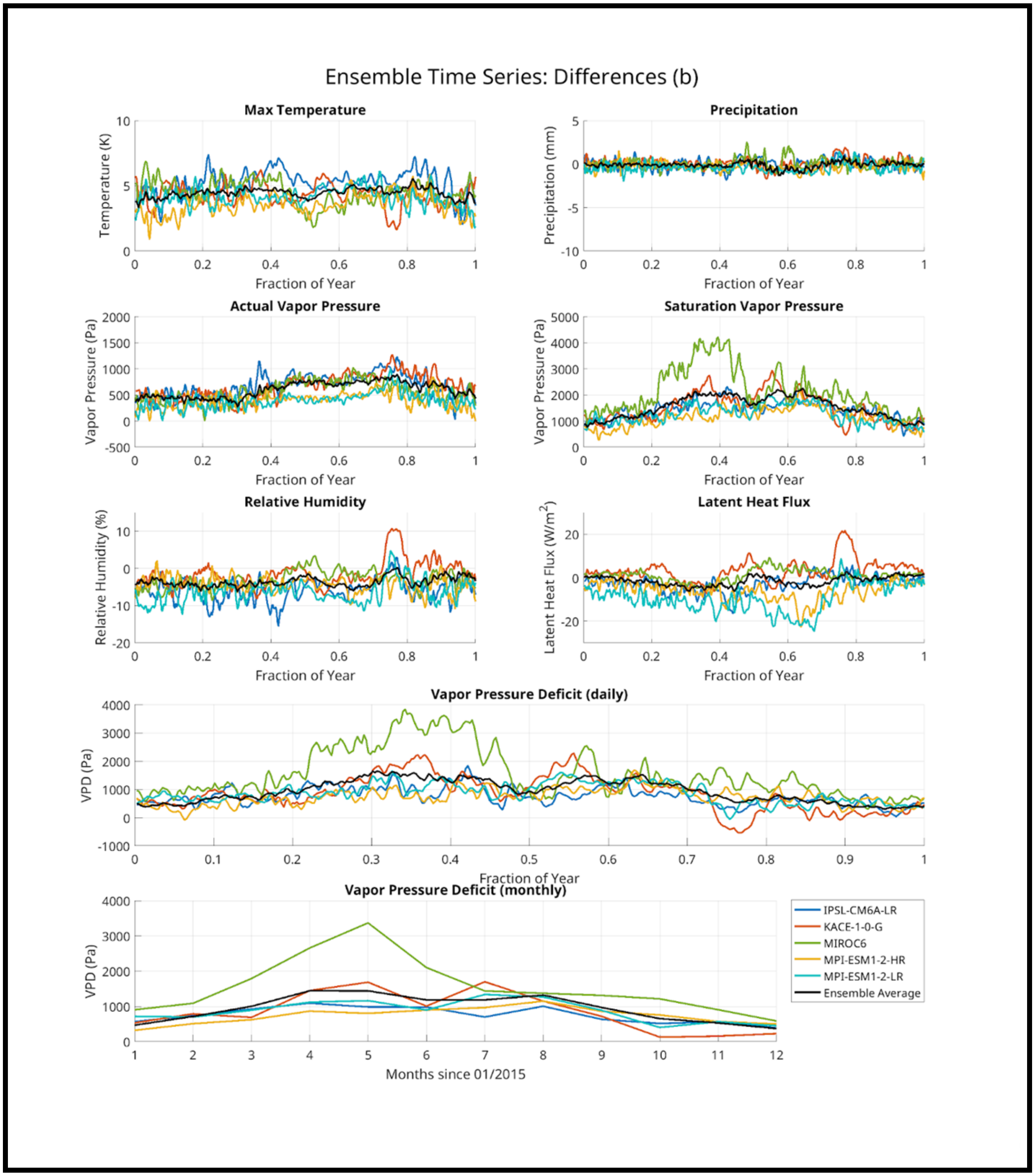

Figure 4.4.4. Ensemble Time Series: Differences (b). Same as in Figure 4.4.3, except with the remaining five models plotted in color, instead.

4.4.1. CanESM5-1

This model shows a suspected NAM signal. Precipitation is near zero with a sudden peak occurring in mid to late June (Figure 4.4.0.1). Despite a clear trend of increasing temperature into July maxima (on average ~ 308K), VPD begins to decrease, just as the rate of increase in temperature begins to flatten out as temperature approaches its maxima. Not shown are the individual first 20 years, however VPD decreases often suddenly with precipitation events, and is generally, relatively low during the extent of the believed NAM and temperature maxima. Extreme year VPD maxima tend to be between 5000 and 7000 Pa, occurring before the start of the high precipitation period (Figure 4.4.1.1). However, VPD is on average at a maxima closer to 4500 Pa (Figure 4.4.1).

In the first 20 years, the actual vapor pressure is slightly above the ensemble average during the period of highest VPD, and shortly after, RH is slightly above during the period of highest temperature (Figure 4.4.1). Precipitation is significantly higher during the period of the suspected monsoon, corresponding to the peak of actual vapor pressure. However, despite the highest precipitation values by nearly double every other model (other than CanESM5, which is very similar to this model), the RH is only marginally higher than the ensemble average and is not the highest of the models, the actual vapor pressure is approximately at the ensemble average, and the VPD is approximately at the ensemble average.

In the last 20 years, temperature increases throughout the entire year by, on average, over 5 K (Figure 4.4.3). As such, and as expected mathematically, saturated vapor pressure shows the temperature trend as an exaggerated, exponential increase. The time period of maximum increase in saturated vapor pressure deficit and VPD (two peaks, but specifically the peak at about .3 years) corresponds to approximately the month of April, whereas the second maxima at about .45 years corresponds to about the period of the three most extremes. This second peak is a sharper increase in VPD from the first 20 years. Precipitation decrease in the last 20 years from the first 20 years is high, and in some places the decreases are by more than half. An important thing to remember is the high variability in the timing and extent of precipitation events, as some decreases are approximately zero.

All three extreme events take place within 30 days of each other (of their respective years), about mid-May. VPD tends to increase with increased temperature, at a maximum of about 5 K to 10 K warmer than the first 20 years of the model run (Figure 4.4.3). The most extreme latent heat flux of the 86-year period occurs during the year of the most extreme VPD, but during the local minima in precipitation of the believed NAM period (about 40 days later) (Figure 4.4.1.1). Temperature gradually increases by about 2 K in the 3-4 days prior to the event, and decreases in a similar gradual behavior following the event. All three of these extreme VPD events are similar in that they take place just prior to assumed NAM precipitation, have somewhat low RH, and have peaks in temperature that are almost the highest or just marginally the highest of the year. Extreme VPD years have similar precipitation to the base state, however being about a month prior may suggest earlier NAM start dates.

The 1st extreme is close to the highest temperature of the year, but not the highest of the 86-year period (Figure 4.4.1.1). Minimal precipitation and near zero values have occurred in the months prior, though the RH and latent heat flux have dipped in the past five or so days prior corresponding to the growth of VPD. The 2nd extreme's temperature is marginally at its highest of the year, though later warm season temperatures remain high. Again, minimal precipitation with near zero values has occurred in the months prior. Changes in relative humidity are subtle, like the temperature signal leading up to the extreme VPD event. During the year of the 3rd extreme, the maximum temperature of the 86-year period occurs, but while it corresponds to a VPD peak, it is slightly below the third maximum VPD event. A clear precipitation signal occurs, responsible for the dip between the peaks in this year. The maximum VPD in this year corresponds to a minimal precipitation with near zero values in months prior.

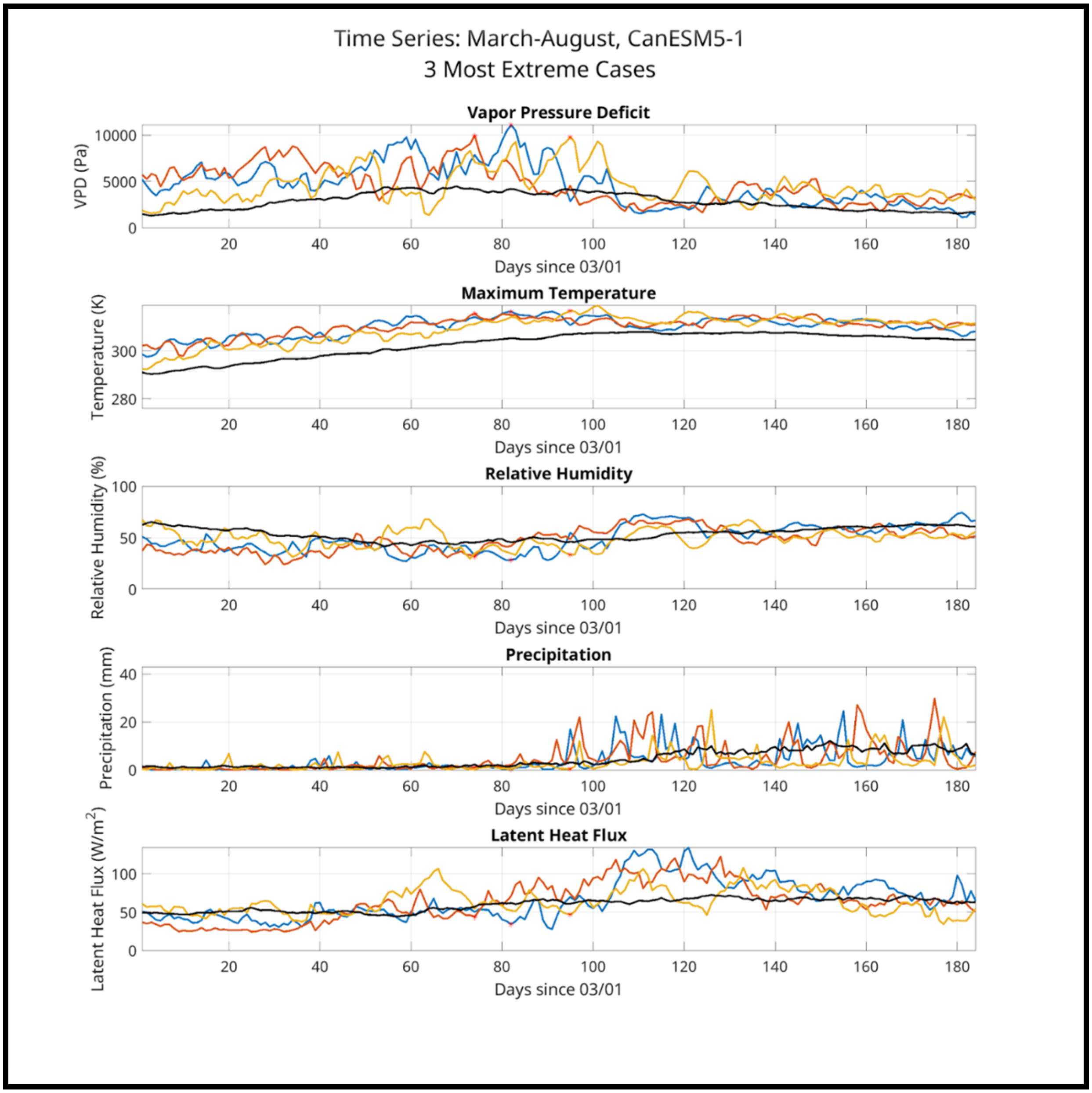

Figure 4.4.1.1. Time Series: March-August, CanESM5-1; 3 Most Extreme Cases. March through August time series for select variables of the three most extreme VPD years (1st extreme: blue, 2nd extreme: red, 3rd extreme: yellow) and the first 20-year average (black) of the CanESM5-1 model. Averages are for the Southwest U.S. and Northern Mexico region, landmasked and latitude weighted.

4.4.2. CanESM5

Like the Canadian model discussed just prior, this model too shows a suspected NAM signal with very similar precipitation behavior. In fact, the average first 20-year behavior of both Canadian models are remarkably similar (Figure 4.4.1). There are no key differences to mention.

There are however key differences from the other Canadian model in the change of the last 20 years from the first 20 years (Figure 4.4.3). This model receives a slightly less decrease in the "extremes" of the precipitation signal (at most, ~ -5 mm). The maximum temperature increasing behavior is similar, however there are variable peaks that are mismatched in dates that lead to the highest changes in VPD being slightly greater, and slightly later in the year.

Despite the slightly later peaks in VPD increase in the last 20 years as compared to the other Canadian model, the dates of this model's events are, if anything, slightly earlier. The behavior of the extreme VPD events is also different (Figure 4.4.2.1.). Again, the temperature corresponding to the maximums are not themselves the maximum by a marginal amount or are the maximum by a marginal amount, correspond to relative low dips in RH, were led by a period of near zero precipitation, followed by suspected NAM precipitation, and take place within 30 days of each other. What differs here is a far more gradual buildup of VPD leading into the event, whereas temperature continues to increase through the event. Latent heat flux is at a near minimum during these events.

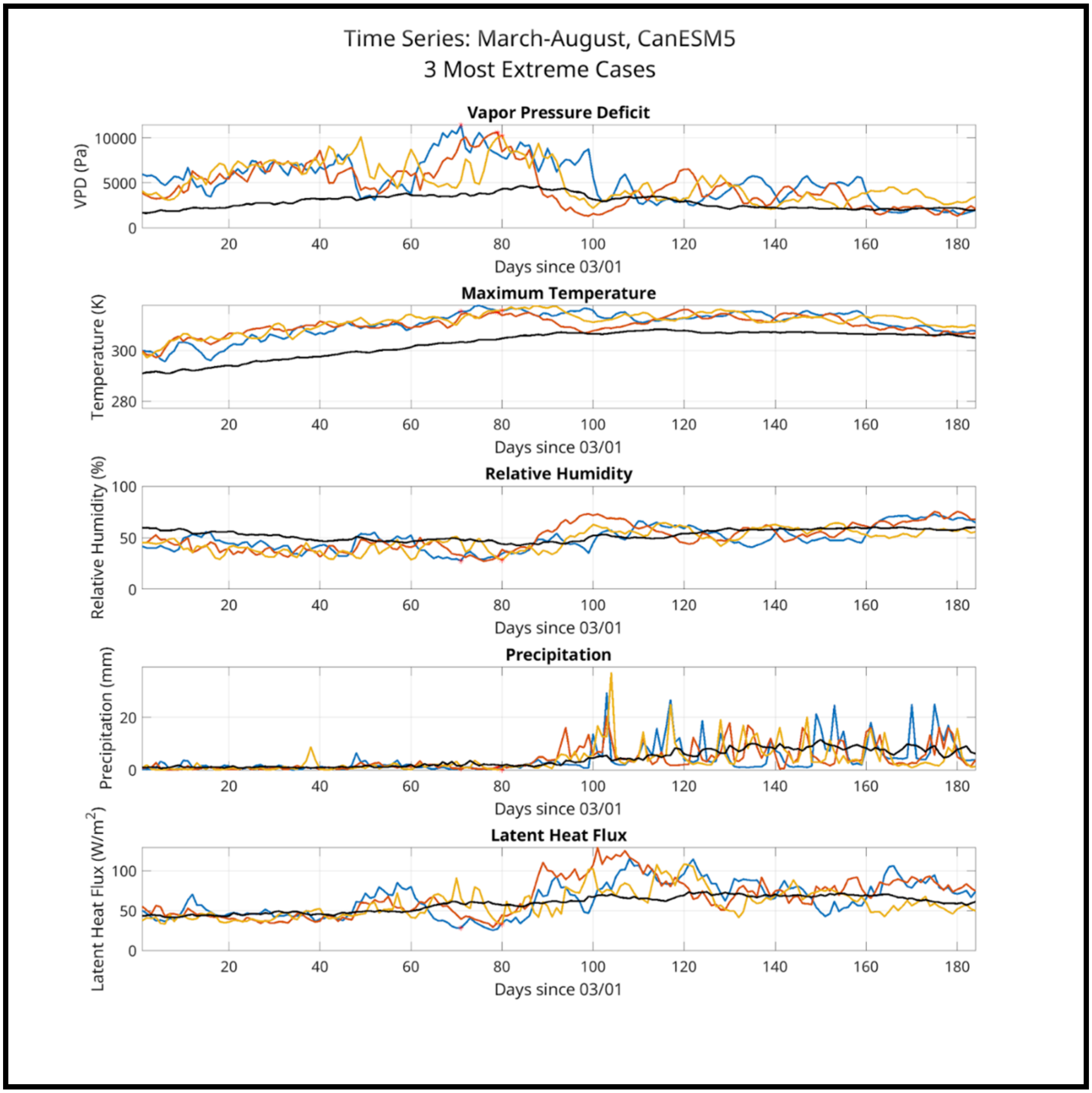

Figure 4.4.2.1. Time Series: March-August, CanESM5; 3 Most Extreme Cases. Same as in Figure 4.4.1.1, except for the CanESM5 model.

4.4.3. INM-CM4-8

The first 20 years of this model are very similar to the Canadian models, following closely to the ensemble averages for all variables, except precipitation (Figure 4.4.1). In this model, precipitation is significantly lower than the ensemble average (dominated by the high Canadian model precipitation values) during the suspected NAM. There is still an increase in precipitation during this period, though it is an increase of no more than a millimeter on average. VPD is higher than the Canadian models following the period of highest extent, displaying a more gradual decrease.

The only variable without much of a change in the last 20 years from the first 20 years is precipitation (Figure 4.4.3). Granted precipitation does decrease slightly in the latter part of the year. Maximum temperature increases across the board, with changes on average about 4 K, being noisy, with a maximum increase peak of about 5.5 K just before .6 years. The saturated vapor pressure peak, and quite intriguing, the actual vapor pressure minimum peak, both align with the temperature peak and maximum VPD peak. RH and latent heat flux decrease across the board in this model by no more than about -10% and -15 W/m^2 respectively. Actual vapor pressure has some near zero changes, but in general, increases by about 500 Pa throughout the year.

VPD extreme events and trends are not within 30 days of each other like the Canadian models, and show more variability in their nature (Figure 4.4.3.1). The precipitation signal is also very low, but never actually zero for the duration of the year in all the three years of high

VPD events.

The most extreme case has VPD at levels on par to those of the first 20 years between about 25 and 10 days prior to the event (temperature is somewhat stable during this).e Temperature began gradually rising about 10 days prior to the event, and increased by roughly 5 K, corresponding to a decrease in RH, and a gradual, yet significant increase in VPD by about 6,500 Pa to its peak of just over 10,000 Pa. The temperature peak corresponding to this event was the highest of the 86-year model run.

The second extreme event is similar to that of the first. The increase in VPD leading into this event also begins at the first 20 year average, and is a steady increase into the peak corresponding to a steady increase in temperature and decrease in RH, where latent heat flux is at a low peak. The temperature corresponding to this VPD event is the highest of its year.

The third highest extreme VPD event takes the behavior of the first two events to a more extreme graduality. VPD leading into this event is once again near (and slightly below in this case) the first 20-year average. However here, this near first 20-year average VPD level is about 45 days prior with a near steady increase in temperature. In this case, temperature peaks about 10 days prior and holds steady while RH falls at a low gradual rate.

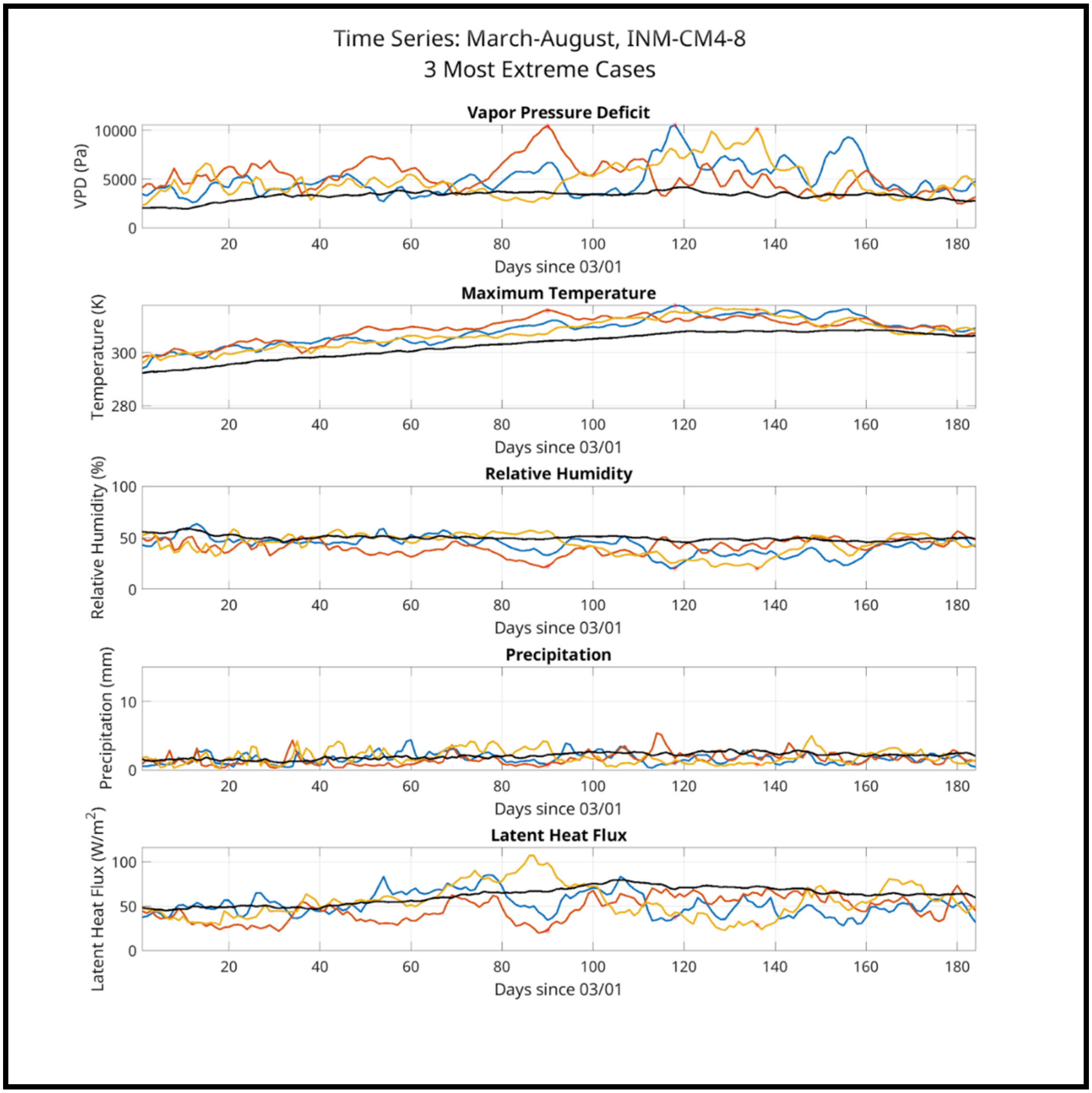

Figure 4.4.3.1. Time Series: March-August, INM-CM4-8; 3 Most Extreme Cases. Same as in Figure 4.4.1.1, except for the INM-CM4-8 model.

4.4.4. INM-CM5-0

As the Canadian models were similar in nature, this Russian model is similar to its Russian counterpart. The changes from the last 20 years to the first 20 years, however, vary from the other Russian model (Figure 4.4.3). The changes in maximum temperature are not as great, reaching a peak of about 4 K just after .6 years with an average increase of roughly 3 K. This peak is however similar with the saturated vapor pressure peak and actual vapor pressure minimum peak both aligning with the temperature and maximum VPD maximum peak. Precipitation shows very little change, with some noisy, slight increases. On average, some days decrease in VPD in the last 20 years relative to the first 20, both in the first three tenths and last two tenths of the year. The increases in VPD are very low in this model relative to the ensemble average in the months February through June, and reach the average increase in August.

The first and second extremes took place in the same year (second extreme dropped to have three unique years) (Figure 4.4.4.1). The three extreme events with unique years took place within 30 days of each other. These are some of the latest events of all the models, being in mid-July through Early August. The dropped event, however, took place in early May. The three events in this model are very similar with exceptionally high temperatures and low RH. Highest VPD corresponded to the temperature peaks, rising gradually with temperature in the days (or week) prior, while RH was lowest for their respective year. The second event did not take place with the highest temperature of the year (yet still being the second highest peak), however this event took place with the lowest RH and latent heat flux. The temperature increased quickly just 3-4 days prior with a gradual increase of about 3-4 K, and corresponds to a rather sharp increase in VPD by about 5000 Pa.

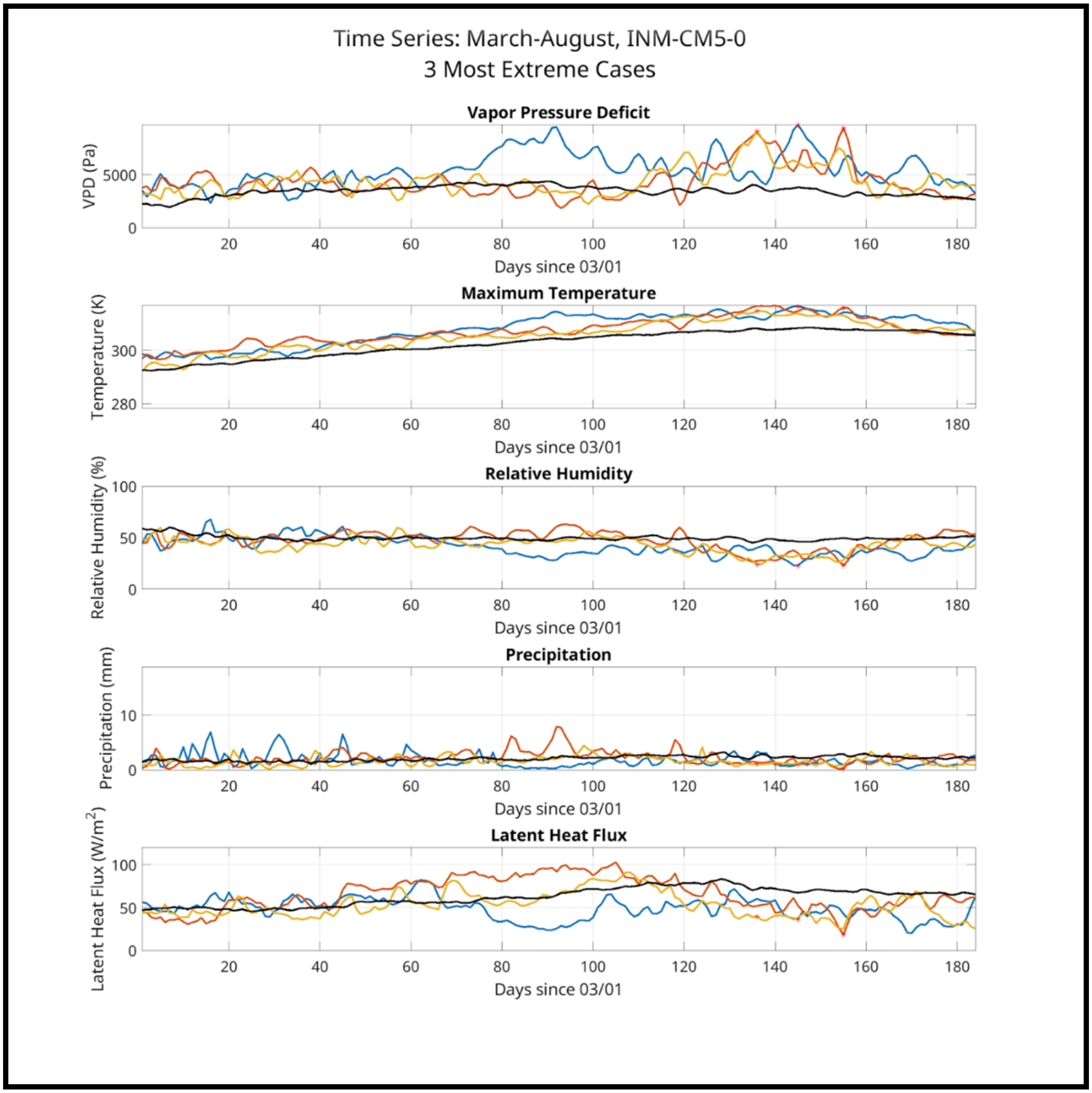

Figure 4.4.4.1. Time Series: March-August, INM-CM5-0; 3 Most Extreme Cases. Same as in Figure 4.4.1.1, except for the INM-CM5-0 model.

4.4.5. IPSL-CM6A-LR

This model has the lowest maximum temperatures, saturation vapor pressures, and VPD of all nine model base states in this study (Figure 4.4.2). As compared to the ensemble average, precipitation is marginally higher with noise, actual vapor pressure is marginally lower throughout, RH is about 5% (at most 10%) throughout, and latent heat flux has a significantly high peak spanning the middle third of the year. This model's latent heat flux dominates the upper distribution of fluxes in the ensemble average.

There is an interesting peak of actual vapor pressure change, increasing in the last 20 years by about 500 Pa, at about .35 years (Figure 4.4.4). This peak is just before the rise of the increasing maximum temperature peak and decreasing minimum RH peak., just after .4 years. Changes in VPD are lower than other models and the ensemble average (considering the monthly averages), but usually not the lowest increases, always increasing. There is a high temperature increase peak at about .25 and .45 years, and four between .8 and .9 years, reaching approximately 7 K. Maximum temperature increase is on average close to 6 K.

The years of extreme VPD events in this model all have multiple VPD-peaking events (Figure 4.4.5.1). The second most extreme event takes place at its year's highest temperature, however the other two events do not. The most extreme and third extreme events take place earlier in the year, relative to the second event and other models, when temperature is 10 K and 5 K lower than the year's maximum, respectively. RH is marginally lower than at the highest temperature periods, however considering the equation for VPD, this means that the actual vapor pressure was lower for these extreme events. All three events show similar behaviors as other models, in that the VPD increases gradually by a significant amount in the handful of days leading into the event.

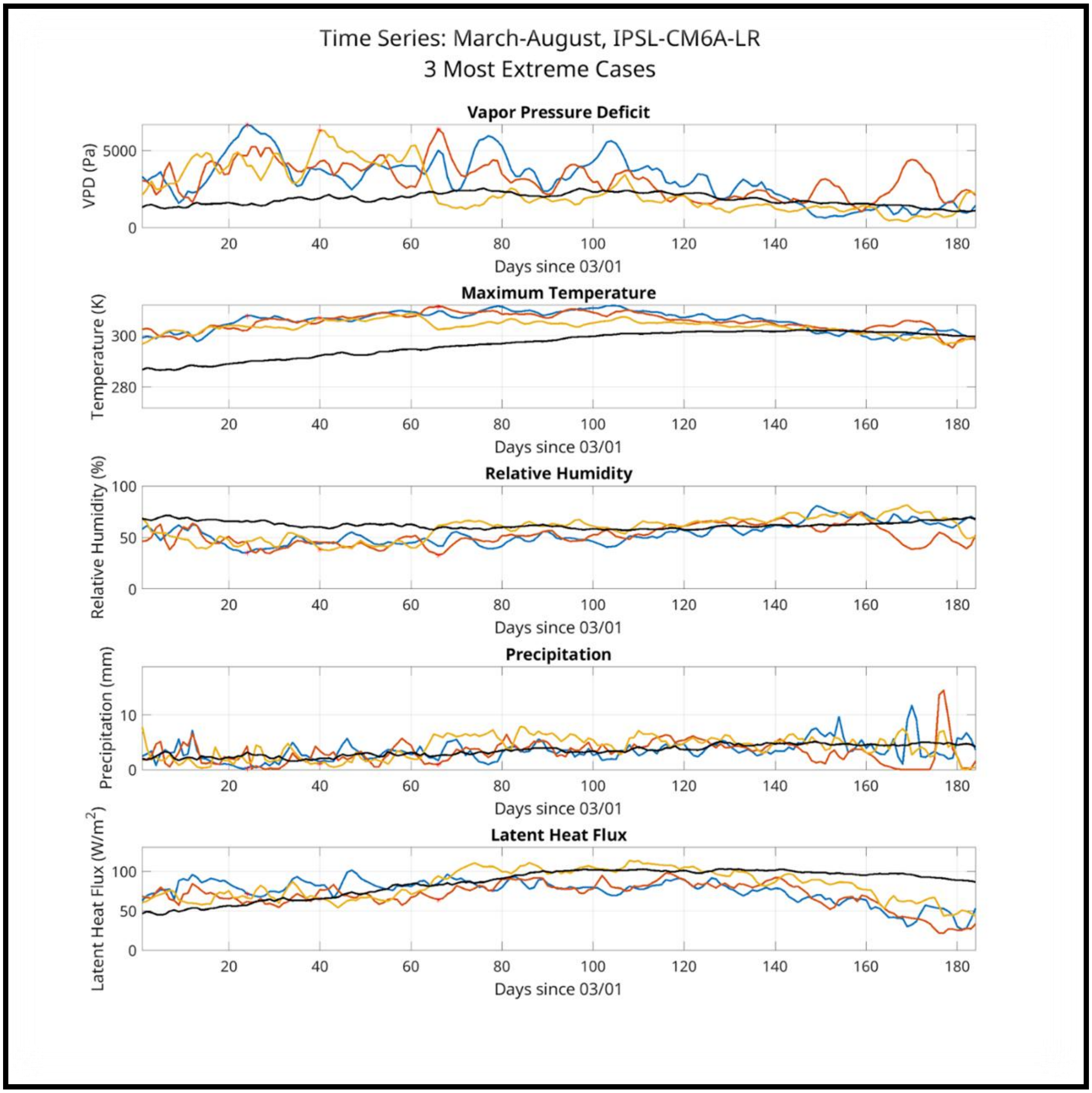

Figure 4.4.5.1. Time Series: March-August, IPSL-CM6A-LR; 3 Most Extreme Cases. Same as in Figure 4.4.1.1, except for the IPSL-CM6A-LR model.

4.4.6. KACE-1-0-G

This model shows a similar maximum temperature trend of the ensemble average in the first 20 years, with the exception of a strong increase about .15 years prior to the ensemble average's peak, having its peak about .1 years prior, and decreasing rapidly back down to the ensemble average's level just prior to the average's peak (Figure 4.4.2). Naturally, saturated vapor pressure follows this same trend. RH has an inverted behavior of this trend in the same manner. Latent heat varies, but also has a low peak during this period. Precipitation shows a rainy season during the expected timing of the NAM, but is 1 to 1.5 mm lower than the ensemble average during this time. Actual vapor pressure is about 250 Pa lower than the ensemble average for the first half of the year. VPD is straightforward here, being higher in the first half of the year while actual vapor pressure is lower (than the ensemble average), with its peak at the peak of maximum temperature.

Changes from the first 20 years shown in this model are apparent (Figure 4.4.4). However, the lineup in time of multiple variables is not as clear cut as in other models. Notably, there are three main periods of VPD change. At about .35 and .55 years are increased peaks, with an ensemble minimum decrease at about .75 years. The decrease in VPD aligns with a stark lower peak in the temperature increase, with stark increases in RH and latent heat flux.

The extreme VPD cases align well with the periods of highest VPD increase from the first 20 years (Figure 4.4.6.1). The second and third cases are similar, in that the significant temperature peaks associated with the events are marginally lower than the highest temperatures of the year. Temperature also rises a good 40 or so days before reaching its peak, following the event (with dips just after the event). Precipitation does show increases (albeit not nearly as high as the Canadian models) in the expected NAM period from a near zero value, and starkly close to zero values leading up to and during the second and third events. The first extreme in this model is unique in respect to its timing. The timing of the most extreme event is during the expected NAM period, however precipitation was near zero for nearly 20 days prior to the event, about 4 mm less than the first 20-year average. During this period, temperatures rise by several degrees than the maximum temperatures of the other two extreme events. The temperature rises by nearly 10 K in this dry period.

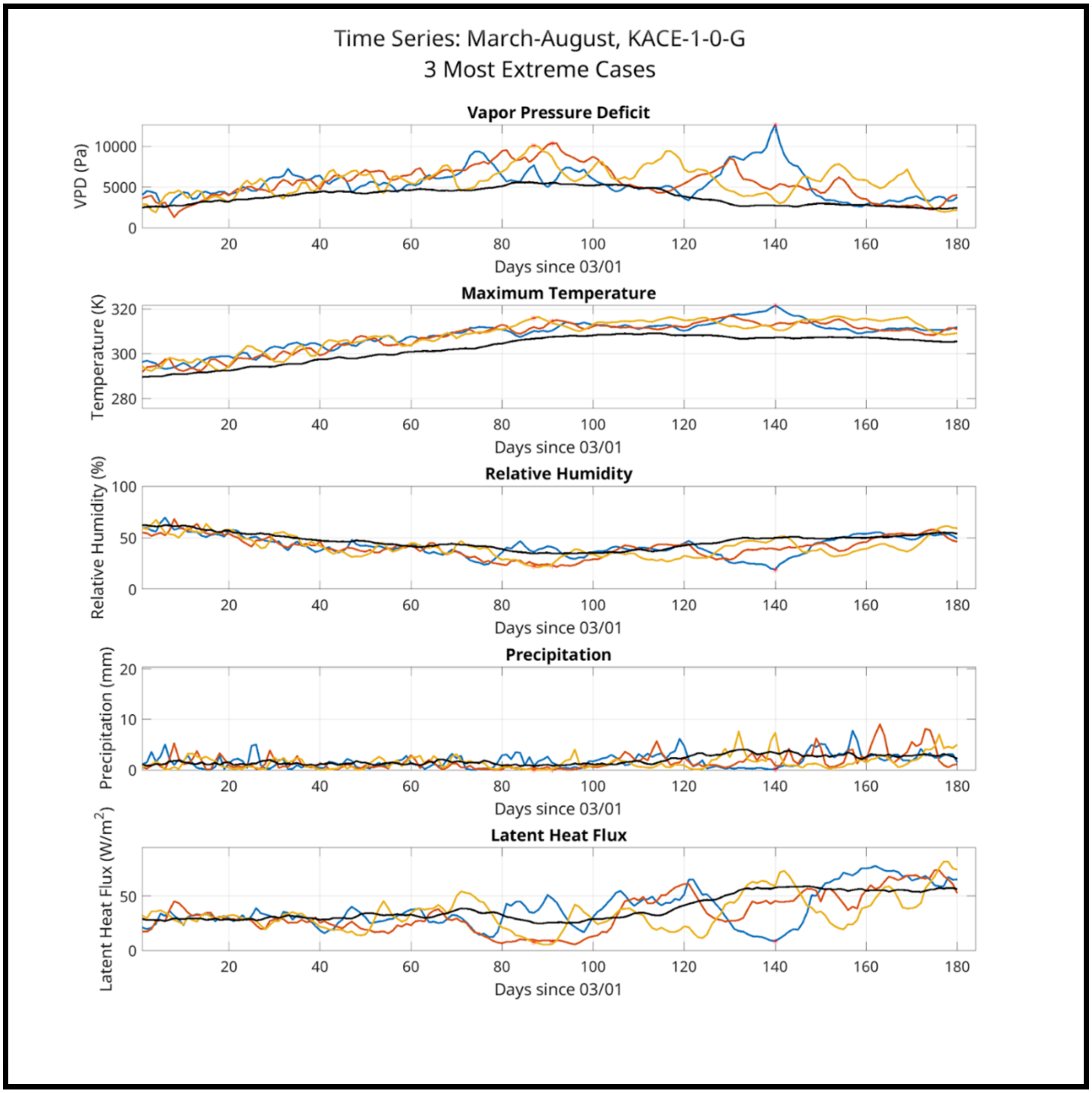

Figure 4.4.6.1. Time Series: March-August, KACE-1-0-G; 3 Most Extreme Cases. Same as in Figure 4.4.1.1, except for the KACE-1-0-G model.

4.4.7. MIROC6

This model shows significantly high base state maximum temperatures, with a first 20 year average higher than most, if not all models in their last 20 years (Rivaled by the Canadian models) (Figure 4.4.2). The average highest, maximum temperature, is about 316 K for the entire region. Along with this are high saturation vapor pressures. Unlike other models, the peak in maximum temperature is ahead of the peak in actual vapor pressure, which is also higher than the ensemble average during the middle two quarters of the year. Still RH is lower than the ensemble average for the entire average first 20-year period. Despite the increased vapor pressure relative to the ensemble average, precipitation is slightly lower than the ensemble average during this period (also being the expected period of the NAM).

Despite the high base state, increases of maximum temperature during the period of high temperature in the first 20 years, are the lowest increases, being the period where changes are below the ensemble average (about .45 to .65 years) (Figure 4.4.4). There are increases in precipitation by a couple millimeters that could explain this. The highest increases in temperature are in the beginning of the year. Saturation vapor pressure increases drastically from about .2 to .5 years, associated with the increases in maximum temperature, but fueled by the high base state and exponential behavior of saturated vapor pressure with temperature. As such, there are drastic increases in VPD during this same period. Actual vapor pressure maintains around the ensemble average in terms of increases. This model has the greatest changes in VPD, in a similar period as the Canadian models, but to a greater extent.

The extreme cases in this model take place within 30 days of each other, and are all of the same nature (Figure 4.4.7.1). The VPD peak is at the peak of temperature for the year, approximately 15 to 20 K higher than the first 20-year average, where temperature remains high for 5 to 10 days, and then gradually decreases down to the first 20-year average near mid-May. All events occur at a minimum of RH with near zero precipitation in the period prior to the events.

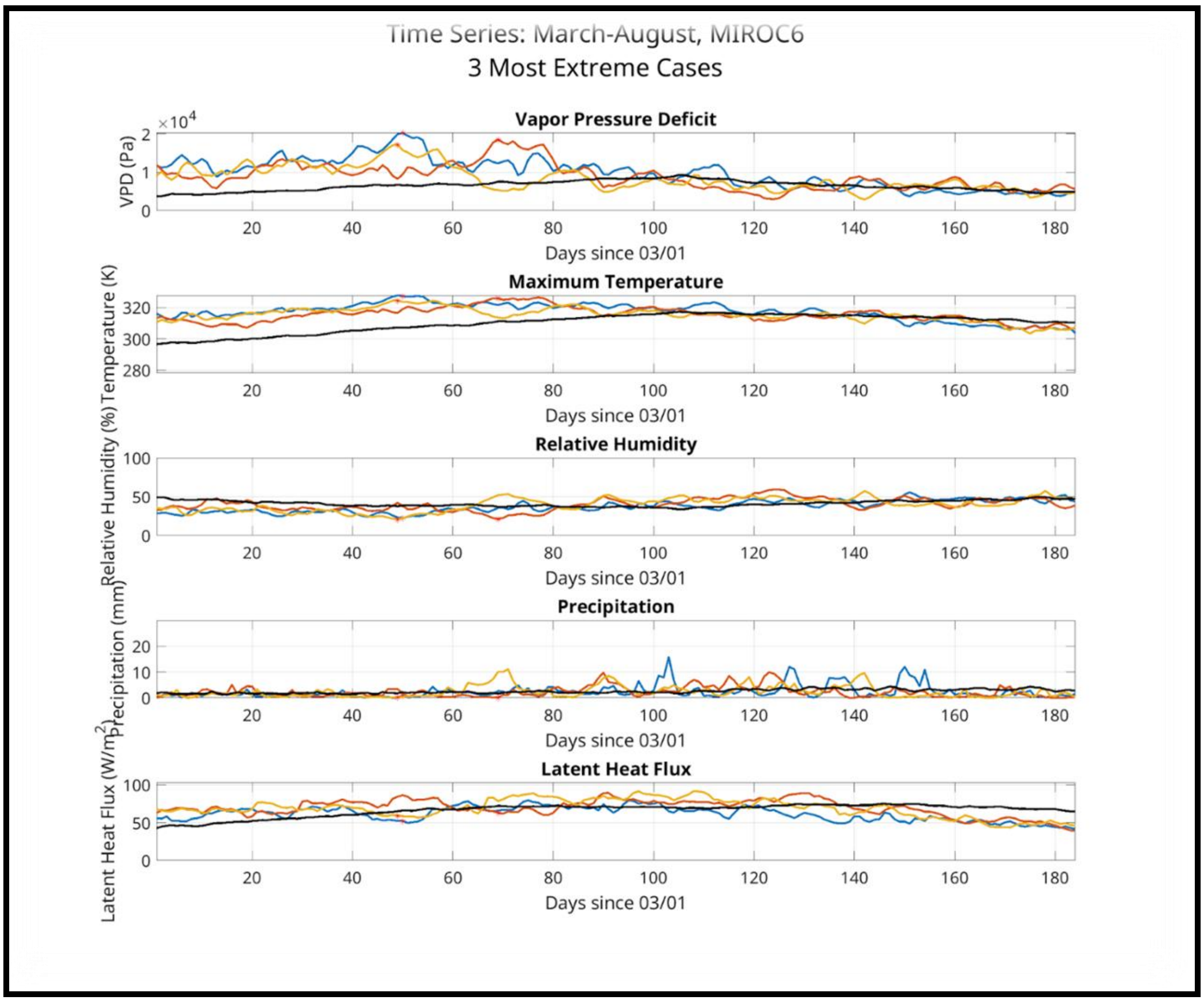

Figure 4.4.7.1. Time Series: March-August, MIROC6; 3 Most Extreme Cases. Same as in Figure 4.4.1.1, except for the MIROC6 model.

4.4.8. MPI-ESM1-2-HR

This model stays predominantly along the ensemble average in the first 20 years, except with precipitation being somewhat low during the suspected NAM period, potentially also having a later NAM start with shorter duration (based solely off of the precipitation time series) (Figure 4.4.2). There is a lower heat flux associated with the lower precipitation.

Increases in temperature from the first 20 years are lower than most other models, being between 4 and 5 K, with peaks in the increase at about .3 years, and between .65 and .85 years (Figure 4.4.4). While precipitation change is approximately that of the ensemble average, the actual vapor pressure differs. Actual vapor pressure increases, but with a noticeable lower extent in the middle of the year. Changes in VPD are on average greater in July and August.

While precipitation in this model and years of extreme VPD are more variable than other models (albeit low levels in comparison to the Canadian models) with a less obvious shift in precipitation during the expected NAM period, the precipitation at and leading up to the events is near zero (Figure 4.4.8.1). Temperature is at a maximum of the respective year for these events. The events occur during peaks in temperature that increase in the days prior, to a greater extent in more days than in other models. The temperature peaks are more of sub-peaks in regards to the noise, and are the gradual yearly peak, ignoring the noise.

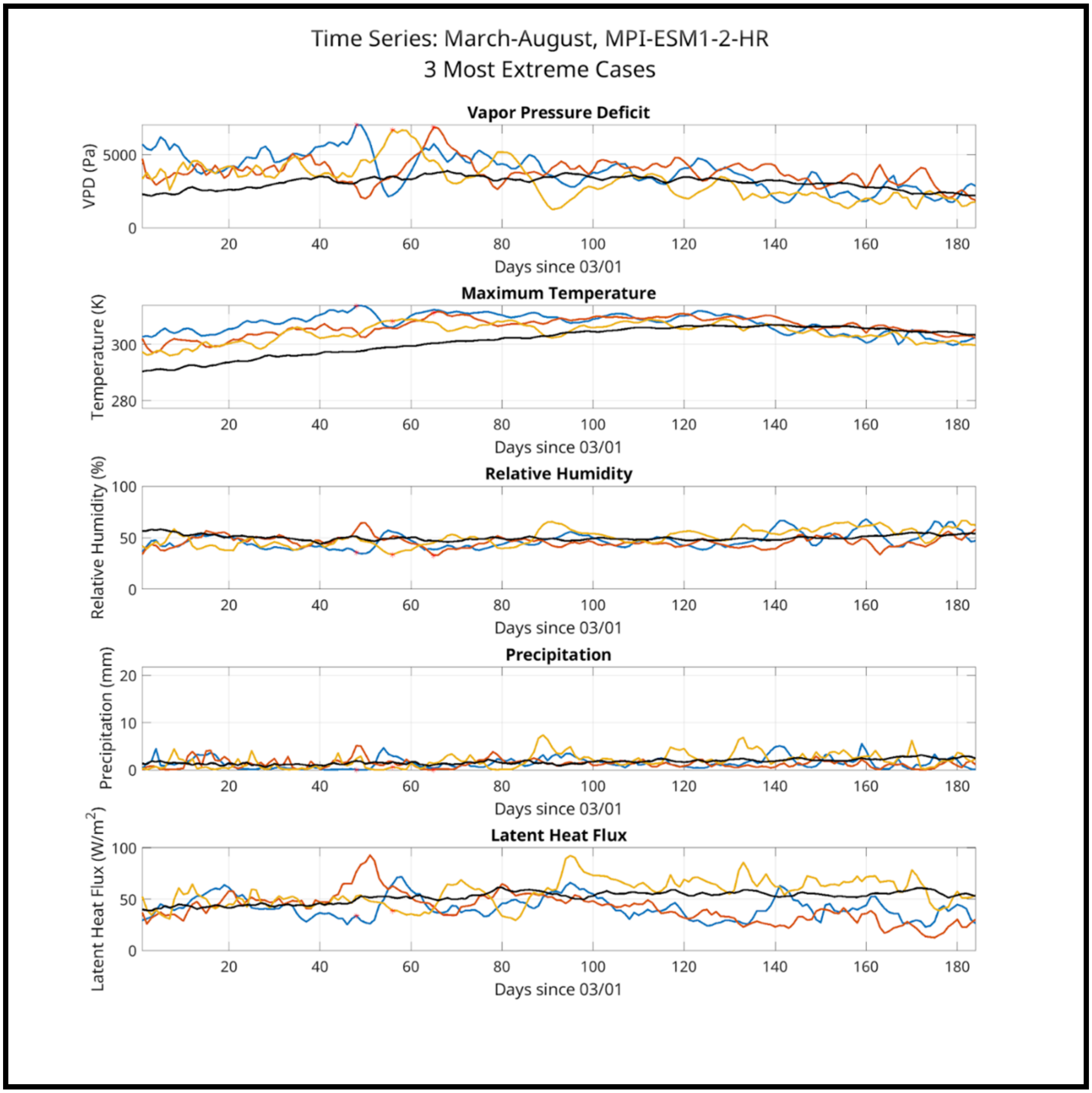

Figure 4.4.8.1. Time Series: March-August, MPI-ESM1-2-HR; 3 Most Extreme Cases. Same as in Figure 4.4.1.1, except for the MPI-ESM1-2-HR model.

4.4.9. MPI-ESM1-2-LR

In the first 20 years, this model's behavior is very similar to its family counterpart discussed prior. with slightly lower maximum temperatures and VPD (Figure 4.4.2). VPD is now, however, less than the ensemble average, on average, for the duration of the year.

Maximum temperatures increase in the latter 20 years, with noise, approximately along the ensemble average, and greater than its family counterpart (Figure 4.4.4). As such, VPD is slightly greater. Actual vapor pressure and precipitation are very similar to its family counterpart as well. However latent heat flux is a greater negative change.

Extremes in this model are considerably earlier than in other models, with the earliest event occurring in February (the second highest extreme VPD event of this model) (Figure 4.4.9.1). Maximum temperatures corresponding to these extreme events are not when temperature is at its peak, instead at sub-peaks nearly 10 K lower than the maximum of the respective years. Despite high VPD during the periods of highest temperature, and similar low peaks in latent heat flux that are on par with the periods of highest temperature, VPD is still highest earlier in the year in this model (at least in the three most extreme years). With low precipitation throughout both the periods of highest VPD and the high VPD appearing during the temperature maximums, it is implied that these extreme cases are a result of a dry air mass likely advected into this region.

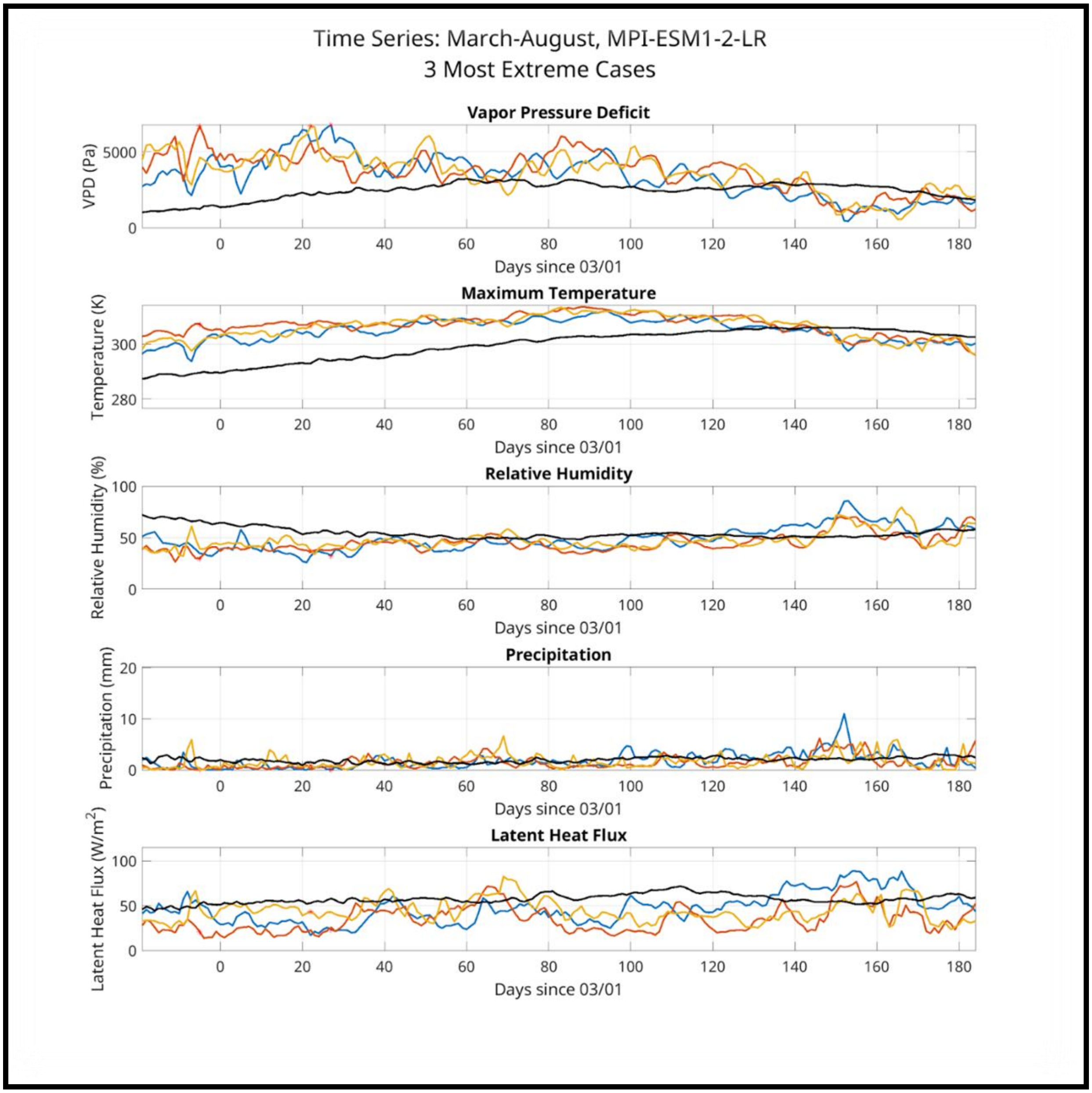

Figure 4.4.9.1. Time Series: March-August, MPI-ESM1-2-LR; 3 Most Extreme Cases. Similar as in Figure 4.4.1.1, except for the MPI-ESM1-2-LR model, and 20 additional days plotted before March 1st (day 0). This is the only model to have an extreme before March 1st. Days before March 1st are given as negative days, starting at zero, for consistency with leap years.

5. Conclusions

Much work has already been completed by researchers to understand vapor pressure deficit in this region, but there are discrepancies between current observations and outputs from climate models in the arid Southwestern North America (Simpson et al., 2023). This study fills gaps in the current literature as the first study to investigate the most extreme cases of VPD in this region within climate model projections. This is accomplished through utilization of daily projections of select meteorological variables. This study also provides a comparison of models' ability to project realistic climatological VPD conditions, based on our current understanding of this region's geography.

Of the 27 extreme VPD events discussed within the nine CMIP6 models under ScenerioMIP8-8.5, patterns do emerge. There are two regions of maximum VPD that develop within the nine climate models. One region of high VPD tends to form in Southern California and spread through the Sonoran Desert. This region tends to be the most extreme with influence from vapor pressure variability. The second region sprawls more broadly through the Great Plains and the Eastern part of the Chihuahuan desert. This region tends to have a lower influence from vapor pressure variability with its spatially sprawling VPD dominated by temperature. Their spatial extent and relation to actual vapor pressure are similar to that of Seager et al. (2015). These two maximas can connect in extreme cases, however they should be studied separately as the nature of the dominating VPD term differs between them.

Based on a time series analysis for the landmasked region, the nine climate models used in this study had extreme events of VPD that fit into three different categories.

1. The first appears in models when temperature is exceptionally high while little change in actual vapor pressure has occurred in the days prior.
2. The second appears with high temperatures that aren't necessarily the highest temperatures of that year, accompanied by decreases in actual vapor pressure.
3. The third appears with exceptional decreases in actual vapor pressure, while temperature is, yes rising, but moderate relative to the rest of the year.

Almost all three cases have gradual increases in VPD with increases in temperature in the days prior, also decreasing somewhat gradually in the subsequent days. Such rates are driven primarily by temperature. The first type is driven almost exclusively by temperature. The second is driven mostly by temperature, with some influence by actual vapor pressure. Type three is driven by actual vapor pressure, to a greater extent than the first three types as this type takes place while temperature is moderate to its yearly maximum.

Type one and two are the most common. When a sudden increase in VPD occurs (on the order of days), it is a type one event. Type one is most extreme if there is an anomalously dry period later in the Summer. Type two events can reach similar extremities as type one, but they take more time to develop, often following approximately a week after a precipitation event occurs, and often showing similar temperature maxima as type one at the time of the event. While temperature rises, actual vapor pressure is also dissipating. Type three is far less common than the first two types of extreme events and tends to occur in earlier Spring. There is a fine line between type one and two, and is subjective to an individual model's climatology.

Precipitation, modelled to different extents in different models, inhibits most extreme VPD cases from being their most extreme (type one events), during the period in the seasonal cycle when solar insolation is at its maximum. Such precipitation is suspected to be driven by the NAM. Models with more active precipitation during the expected NAM period tend to have VPD extremes associated with higher temperatures (not necessarily the highest temperatures) prior to large precipitation events, such as the expected NAM events. All cases occur when precipitation is near zero, though some models seem to model precipitation differently, in which values of near zero simply means low values. This tends to hold true with cases later in the year, being more extreme than earlier cases during periods in which the precipitation is anomalously near zero.

Precipitation moderating temperature in this location is exemplified in the Canadian models, with VPD dipping below the ensemble average when precipitation is significantly greater. The ability of these models to resolve the NAM has not been investigated, though it is suspected to appear in most models during the somewhat expected period of the NAM. Granted, while this study has put a broad level of importance to the NAM, some areas in the region of interest for this study are known to be affected more significantly than others, also varying by monsoon strength. To fully understand projections of VPD into the future, and ensure the physical accuracy of projections, a thorough investigation of precipitation fluxes for this region is necessary.

Suspected NAM precipitation signals are observed within the climate models. However, to say that such a signal is present and attributable to the NAM in any one given year requires more information than just a timeseries. A study determining the source of moisture variability, and importantly precipitation into the Southwest U.S. and Northern Mexico for these CMIP6 experiments is warranted. An assumed North American Monsoon is present in most models, however several models have relatively weak signals. Verifying that the spatial and absolute extent of precipitation show realistic trends relative to the now first 10 years of model runs that have been recorded with observations will provide a level of confidence in the projections.

Conveniently, at time of writing, there is data availability of upper-level meteorological variables for all nine models used in this study. A study on the synoptic meteorology of extreme VPD events within these nine models would shed light into the spatial development of VPD when extreme cases occur. Understanding the spatial extent of VPD provides insight to potential spatial extent of heat, drought, and wildfires, all of which impact large populations in this region. Warranted by this, a study on the synoptic meteorology of extreme VPD events should first verify the sources of moisture variability to this region. The nine models have varying precipitation signals, both on an average and year to year basis. To properly understand the deficit of vapor pressure in this region through models, one should first understand the sources of vapor pressure within each model.

6. References

Adams, D. K., & Comrie, A. C. (1997). The North American Monsoon. *Bulletin of the American Meteorological Society*, *78*(10), 2197–2214. https://doi.org/10.1175/1520-0477(1997)078<2197:TNAM>2.0.CO;2

Alduchov, O. A., & Eskridge, R. E. (1996). Improved Magnus Form Approximation of Saturation Vapor Pressure. *Journal of Applied Meteorology and Climatology*, *35*(4), 601–609. https://doi.org/10.1175/1520-0450(1996)035<0601:IMFAOS>2.0.CO;2

Anderson, D. B. (1936). Relative Humidity or Vapor Pressure Deficit. *Ecology*, *17*(2), 277–282. https://doi.org/10.2307/1931468

Bolton, D. (1980). The Computation of Equivalent Potential Temperature. *Monthly Weather Review*, *108*(7), 1046–1053. https://doi.org/10.1175/1520-0493(1980)108<1046:TCOEPT>2.0.CO;2

Brazel, A. J., & Nickling, W. G. (1986). The relationship of weather types to dust storm generation in Arizona (1965–1980). *Journal of Climatology*, *6*(3), 255–275. https://doi.org/10.1002/JOC.3370060303

Carleton, A. M., Carpenter, D. A., & Weser, P. J. (1990). Mechanisms of Interannual Variability of the Southwest United States Summer Rainfall Maximum. *Journal of Climate*, *3*(9), 999–1015. https://doi.org/10.1175/1520-0442(1990)003<0999:MOIVOT>2.0.CO;2

Ciancarelli, B., Castro, C. L., Woodhouse, C., Dominguez, F., Chang, H.-I., Carrillo, C., & Griffin, D. (2013). Dominant patterns of US warm season precipitation variability in a fine resolution observational record, with focus on the southwest. *INTERNATIONAL JOURNAL OF CLIMATOLOGY Int. J. Climatol*. https://doi.org/10.1002/joc.3716

CMIP6_CVs/CMIP6_grid_label.json at main · WCRP-CMIP/CMIP6_CVs · GitHub. (n.d.). Retrieved June 8, 2025, from https://github.com/WCRP-CMIP/CMIP6_CVs/blob/main/CMIP6_grid_label.json

CMIP6_global_attributes_filenames_CVs - Google Docs. (n.d.). Retrieved June 8, 2025, from https://docs.google.com/document/d/1h0r8RZr_f3-8egBMMh7aqLwy3snpD6_MrDz1q8n5XUk/edit?tab=t.0

Conservation Biology Institute. (n.d.). Retrieved June 8, 2025, from https://databasin.org/maps/new/#datasets=588bcc4e1f2646e589e0fc9593498e3d

Coumou, D., & Robinson, A. (2013). Historic and future increase in the global land area affected by monthly heat extremes. *Environmental Research Letters*, *8*(3), 034018. https://doi.org/10.1088/1748-9326/8/3/034018

Eyring, V., Bony, S., Meehl, G. A., Senior, C. A., Stevens, B., Stouffer, R. J., & Taylor, K. E. (2016a). Overview of the Coupled Model Intercomparison Project Phase 6 (CMIP6) experimental design and organization. *Geoscientific Model Development*, *9*(5), 1937–1958. https://doi.org/10.5194/GMD-9-1937-2016

Eyring, V., Bony, S., Meehl, G. A., Senior, C. A., Stevens, B., Stouffer, R. J., & Taylor, K. E. (2016b). Overview of the Coupled Model Intercomparison Project Phase 6 (CMIP6) experimental design and organization. *Geoscientific Model Development*, *9*(5), 1937–1958. https://doi.org/10.5194/GMD-9-1937-2016

Goff, J. A., and S. Gratch (1945), Thermodynamics properties of moist air, Trans. Am. Soc. Heat. Vent. Eng., 51, 125 – 157.

Gutzler, D. S., Kann, D. M., & Thornbrugh, C. (2002). Modulation of ENSO-Based Long-Lead Outlooks of Southwestern U.S. Winter Precipitation by the Pacific Decadal Oscillation. *Weather and Forecasting*, *17*(6), 1163–1172. https://doi.org/10.1175/1520-0434(2002)017<1163:MOEBLL>2.0.CO;2

Hafner, D. J., & Riddle, B. R. (2011). Boundaries and barriers of North American warm deserts: An evolutionary perspective. *Palaeogeography and Palaeobiogeography: Biodiversity in Space and Time*, 75–113. https://doi.org/10.1201/B11176-10

He, Q., Williams, A. P., Johnston, M. R., Juang, C. S., & Wang, B. (2025). Influence of Time-Averaging of Climate Data on Estimates of Atmospheric Vapor Pressure Deficit and Inferred Relationships With Wildfire Area in the Western United States. *Geophysical Research Letters*, *52*(7), e2024GL113708. https://doi.org/10.1029/2024GL113708

Hermann, M., Wernli, H., & Röthlisberger, M. (2024). Drastic increase in the magnitude of very rare summer-mean vapor pressure deficit extremes. *Nature Communications*, *15*(1), 1–11. https://doi.org/10.1038/S41467-024-51305-W

Hersbach, H., Bell, B., Berrisford, P., Biavati, G., Horányi, A., Muñoz Sabater, J., Nicolas, J., Peubey, C., Radu, R., Rozum, I., Schepers, D., Simmons, A., Soci, C., Dee, D., Thépaut, J-N. (2023b). ERA5 hourly data on single levels from 1940 to present. Copernicus Climate Change Service (C3S) Climate Data Store (CDS). https:/doi.org/10.24381/cds.adbb2d47Huang, J. (2018). A Simple Accurate Formula for Calculating Saturation Vapor Pressure of Water and Ice. *Journal of Applied Meteorology and Climatology*, *57*(6), 1265–1272. https://doi.org/10.1175/JAMC-D-17-0334.1

Iles, C. E., Vautard, R., Strachan, J., Joussaume, S., Eggen, B. R., & Hewitt, C. D. (2020). The benefits of increasing resolution in global and regional climate simulations for European climate extremes. *Geoscientific Model Development*, *13*(11), 5583–5607. https://doi.org/10.5194/GMD-13-5583-2020

Jaffe, D. A., O'Neill, S. M., Larkin, N. K., Holder, A. L., Peterson, D. L., Halofsky, J. E., & Rappold, A. G. (2020). Wildfire and prescribed burning impacts on air quality in the United States. *Journal of the Air & Waste Management Association*, *70*(6), 583–615. https://doi.org/10.1080/10962247.2020.1749731

Kretzschmar, H. J., & Wagner, W. (2019). International steam tables: Properties of water and steam based on the industrial formulation IAPWS-IF97. *International Steam Tables: Properties of Water and Steam Based on the Industrial Formulation IAPWS-IF97*, 1–380. https://doi.org/10.1007/978-3-662-53219-5

Liu, S., Hu, S., & Seager, R. (2024). The West Pacific Teleconnection Drives the Interannual Variability of Autumn Wildfire Weather in the Western United States After 2000. *Earth's Future*, *12*(11), e2024EF004922. https://doi.org/10.1029/2024EF004922

Maddox, R. A., McCollum, D. M., & Howard, K. W. (1995). Large-Scale Patterns Associated with Severe Summertime Thunderstorms over Central Arizona. *Weather and Forecasting*, *10*(4), 763–778. https://doi.org/10.1175/1520-0434(1995)010<0763:LSPAWS>2.0.CO;2

Meinshausen, M., Nicholls, Z. R. J., Lewis, J., Gidden, M. J., Vogel, E., Freund, M., Beyerle, U., Gessner, C., Nauels, A., Bauer, N., Canadell, J. G., Daniel, J. S., John, A., Krummel, P. B., Luderer, G., Meinshausen, N., Montzka, S. A., Rayner, P. J., Reimann, S., … Wang, R. H. J. (2020). The shared socio-economic pathway (SSP) greenhouse gas concentrations and their extensions to 2500. *Geoscientific Model Development*, *13*(8), 3571–3605. https://doi.org/10.5194/GMD-13-3571-2020

Mo, K. C., & Paegle, J. N. (2000). Influence of Sea Surface Temperature Anomalies on the Precipitation Regimes over the Southwest United States. *Journal of Climate*, *13*(20), 3588–3598. https://doi.org/10.1175/1520-0442(2000)013<3588:IOSSTA>2.0.CO;2

Moreno-Chamarro, E., Caron, L. P., Loosveldt Tomas, S., Vegas-Regidor, J., Gutjahr, O., Moine, M. P., Putrasahan, D., Roberts, C. D., Roberts, M. J., Senan, R., Terray, L., Tourigny, E., & Vidale, P. L. (2022). Impact of increased resolution on long-standing biases in HighResMIP-PRIMAVERA climate models. *Geoscientific Model Development*, *15*(1), 269–289. https://doi.org/10.5194/GMD-15-269-2022

Mueller, S. E., Thode, A. E., Margolis, E. Q., Yocom, L. L., Young, J. D., & Iniguez, J. M. (2020). Climate relationships with increasing wildfire in the southwestern US from 1984 to 2015. *Forest Ecology and Management*, *460*, 117861. https://doi.org/10.1016/J.FORECO.2019.117861

Murray, F. W. (1967). On the Computation of Saturation Vapor Pressure. *Journal of Applied Meteorology and Climatology*, *6*(1), 203–204. https://doi.org/10.1175/1520-0450(1967)006<0203:OTCOSV>2.0.CO;2

Navarro-Racines, C., Tarapues, J., Thornton, P., Jarvis, A., & Ramirez-Villegas, J. (2020). High-resolution and bias-corrected CMIP5 projections for climate change impact assessments. *Scientific Data*, *7*(1), 1–14. https://doi.org/10.1038/S41597-019-0343-8

North American Monsoon Highlights. (n.d.). Retrieved June 8, 2025, from https://www.weather.gov/abq/northamericanmonsoon-intro

O'neill, B. C., Tebaldi, C., Van Vuuren, D. P., Eyring, V., Friedlingstein, P., Hurtt, G., Knutti, R., Kriegler, E., Lamarque, J.-F., Lowe, J., Meehl, G. A., Moss, R., Riahi, K., & Sanderson, B. M. (2016). The Scenario Model Intercomparison Project (ScenarioMIP) for CMIP6. *Geosci. Model Dev*, *9*, 3461–3482. https://doi.org/10.5194/gmd-9-3461-2016

Records of Weather and Climate Extremes Table. (n.d.). Retrieved June 8, 2025, from https://wmo.int/files/records-of-weather-and-climate-extremes-table?book=21486

Seager, R., Hooks, A., Williams, A. P., Cook, B., Nakamura, J., & Henderson, N. (2015). Climatology, Variability, and Trends in the U.S. Vapor Pressure Deficit, an Important Fire-Related Meteorological Quantity. *Journal of Applied Meteorology and Climatology*, *54*(6), 1121–1141. https://doi.org/10.1175/JAMC-D-14-0321.1

Sheppard, P. R., Comrie, A. C., Packin, G. D., Angersbach, K., & Hughes, M. K. (2002). The climate of the US Southwest. *Climate Research*, *21*(3), 219–238. https://doi.org/10.3354/CR021219

Simpson, I. R., McKinnon, K. A., Kennedy, D., Lawrence, D. M., Lehner, F., & Seager, R. (2024). Observed humidity trends in dry regions contradict climate models. *Proceedings of the National Academy of Sciences of the United States of America*, *121*(1), e2302480120. https://doi.org/10.1073/PNAS.2302480120

Soulé, P. T., & Knapp, P. A. (2024). The evolution of "Hot" droughts in Southern California, USA from the 20th to the 21st century. *Journal of Arid Environments*, *220*, 105118. https://doi.org/10.1016/J.JARIDENV.2023.105118

Stensrud, D. J., Gall, R. L., & Nordquist, M. K. (1997). Surges over the Gulf of California during the Mexican Monsoon. *Monthly Weather Review*, *125*(4), 417–437. https://doi.org/10.1175/1520-0493(1997)125<0417:SOTGOC>2.0.CO;2

Svoboda, M., LeComte, D., Hayes, M., Heim, R., Gleason, K., Angel, J., Rippey, B., Tinker, R., Palecki, M., Stooksbury, D., Miskus, D., & Stephens, S. (2002). THE DROUGHT MONITOR. *Bulletin of the American Meteorological Society*, *83*(8), 1181–1190. https://doi.org/10.1175/1520-0477-83.8.1181

Van Wagner, C. E. . (1987). *Development and structure of the Canadian Forest Fire Weather Index System*. Canadian Forestry Service. https://ostrnrcan-dostrncan.canada.ca/handle/1845/228434

Wallace, J. M., & Gutzler, D. S. (1981). Teleconnections in the Geopotential Height Field during the Northern Hemisphere Winter. *Monthly Weather Review*, *109*(4), 784–812. https://doi.org/10.1175/1520-0493(1981)109<0784:TITGHF>2.0.CO;2

Wexler, A. (1976). Vapor Pressure Formulation for Water in Range 0 to 100 °C. A Revision. *Journal of Research of the National Bureau of Standards. Section A, Physics and Chemistry*, *80A*(5–6), 775. https://doi.org/10.6028/JRES.080A.071

Wildfires and Climate Change - NASA Science. (n.d.). Retrieved June 8, 2025, from https://science.nasa.gov/earth/explore/wildfires-and-climate-change/

Williams, A. P., Cook, B. I., & Smerdon, J. E. (2022). Rapid intensification of the emerging southwestern North American megadrought in 2020–2021. *Nature Climate Change*, *12*(3), 232–234. https://doi.org/10.1038/S41558-022-01290-Z

You, Y., & Ting, M. (2023). Improved Performance of High-Resolution Climate Models in Simulating Asian Monsoon Rainfall Extremes. *Geophysical Research Letters*, *50*(5), e2022GL100827. https://doi.org/10.1029/2022GL100827

Zhuang, Y., Fu, R., Santer, B. D., Dickinson, R. E., & Hall, A. (2021). Quantifying contributions of natural variability and anthropogenic forcings on increased fire weather risk over the western United States. *Proceedings of the National Academy of Sciences of the United States of America*, *118*(45), e2111875118. https://doi.org/10.1073/PNAS.2111875118

7. Appendix

A repository containing the MATLAB code files written for this study can be found on the following GitHub repository: https://github.com/LaForzaDelDestino/Masters-Thesis